

Grantecan spectroscopic observations and confirmations of Planetary Nebulae candidates in the Northern Galactic Plane

A. Ritter,^{1,2} Q. A. Parker^{1,2*}, L. Sabin,³, P. Le Dû^{4,5}, L. Mulato^{4,6}, D. Patchick⁷

¹ The Department of Physics, CYM Physics Laboratory, The University of Hong Kong, Hong Kong (S.A.R.)

²Laboratory for Space Research, The University of Hong Kong, Room 405b, Cyberport 4, 100 Cyberport Rd, Hong Kong (S.A.R.)

³Instituto de Astronomía, Universidad Nacional Autónoma de México, Apdo. Postal 106, 22800 Ensenada, B.C., Mexico

⁴SPOT, 38690 Chabons, France

⁵Kermerrien Observatory, 29840 Porspoder, France

⁶Cornillon Observatory, 30630 Cornillon, France

⁷Deep Sky Hunters Consortium, 90025 Los Angeles, USA

Accepted XXX. Received YYY; in original form ZZZ

ABSTRACT

We present Grantecan 10 m telescope (GTC) spectroscopic confirmations of 55 faint Planetary Nebulae (PNe) candidates discovered largely in the INT Photometric H α Survey of the Northern Galactic Plane (IPHAS) by our pro-am collaboration. We confirm 46 of them as ‘True’ (T), 4 as ‘Likely’ (L) and 5 as ‘Possible’ (P) PNe and including 5 new PNe central star (CSPN) discoveries. This was from observations of 62 new candidates yielding a maximum PN discovery success rate of 89%. The sensitivity and longer wavelength coverage of IPHAS allows PNe to be found in regions of greater extinction and at these lower Galactic latitudes, including PNe in a more advanced evolutionary state and at larger distances compared to previously known Galactic PNe. We use an holistic set of observed characteristics and optical emission-line diagnostics to confirm candidates. Plasma properties have been determined in a self-consistent way using PyNeb. This work is facilitated by the functionality of our powerful, multi-wavelength database ‘HASH’ (Hong Kong, Australian Astronomical Observatory, Strasbourg Observatory H-alpha Planetary Nebula catalogue) that federates known imaging, spectroscopy and other pertinent data for all Galactic T, L, P PNe and the significant numbers of mimics. Reddenings, corrected radial velocities and PNe electron density and temperature estimates are provided for these new PNe where possible.

Key words: planetary nebulae: general – techniques: imaging – techniques: spectroscopic – Astronomical data bases: catalogues

1 INTRODUCTION

Planetary Nebulae (PNe) are the expanding shells of ionized gas ejected from low- to intermediate-mass stars (~ 1 to $8 M_{\odot}$) towards the end of their lives. They are powerful astrophysical tools for studying late stage stellar evolution (Kwitter & Henry 2022) and plasma physics (Hajduk et al. 2021), as well as investigating the chemical evolution of the whole Galaxy (Dopita et al. 1997; Maciel & Costa 2003). Due to their very bright emission lines they can be observed to great distances across our own galaxy and detected and traced in other nearby galaxies in the local group and beyond.

Since Charles Messier observed the first PN (Dumbbell Nebula in Vulpecula) in 1764, over three thousand eight hundred of these beautiful objects have now been discovered in our Galaxy (Parker et al. 2016). Before the advent of the SHS (Parker et al. 2005) and IPHAS (Drew et al. 2005) narrow-band H α surveys of the Southern and Northern Galactic Planes respectively, the vast majority of the previously known PNe ($\sim 1,500$) were compiled from over 200 years of observations from a wide variety of telescopes and spectrographs into the Strasbourg-ESO Catalogue and its supplement (Acker et al. 1992, 1996), and the largely overlapping but indepen-

dent compendium of Kohoutek Kohoutek (2001). However, these new H α surveys led to a more than doubling of known Galactic PNe as reported in Parker et al. (2006); Miszalski et al. (2008) for the Southern Galactic plane and Sabin et al. (2014) for the Northern Galactic plane. These ‘new’ PNe were not simply more of the same but are generally fainter, more evolved/extended, more obscured and also, in many cases, more compact compared to the previous catalogues. Other notable numbers of new PNe discoveries have also come from the Deep Sky Hunters (DSH) ‘amateur’ consortium and more recently from a dedicated group of French amateurs, e.g. Acker et al. (2012). This is via painstaking, fresh analysis of the now online broad and narrow-band Digital Sky Survey plates, e.g. Jacoby et al. (2010), Kronberger et al. (2006, 2012, 2014). This includes our own recent professional-amateur (pro-am) collaboration (Le Dû et al., A&A, in press) that reports the discovery of 210 PNe. Many of these new discoveries are from outside the narrow Galactic latitude confines of the Milky-Way H α surveys (ie $\sim \pm 10$ degrees for the SHS and ± 5 degrees for IPHAS). We are indeed currently in a new golden age of PN discovery in our own Galaxy where pro-am collaborations are playing an increasingly important role with their access to bespoke, dedicated facilities and time.

* E-mail: quentinp@hku.hk

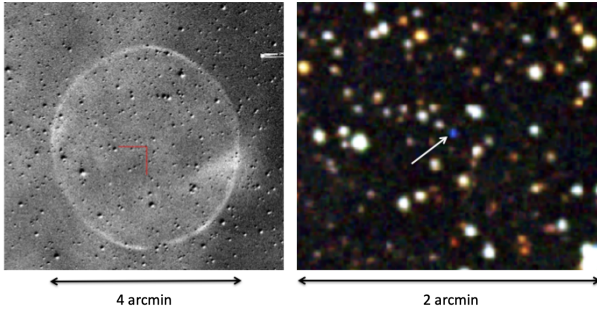


Figure 1. Left panel: Quotient image of a newly confirmed PNe ‘Ju 1’ (HASH ID 4408) that has a diameter of $240''$ and with the position of the independently discovered CSPN indicated by a half-cross in red. The quotient is obtained by dividing the IPHAS H α image by the equivalent broad-band R (red) image. Right panel: A 2×2 arcminute RGB broad band image created from the ‘SSS’ (Hambly et al. 2001) i-band, r-band and B $_J$ band deep photographic data centred on the faint, blue CSPN (arrowed).

2 OBSERVATIONS

A total of 62 new PN candidates were found by careful scrutiny of the IPHAS survey data and other data for more “out of plane” candidates by our combined pro-am team. A total of 55 subsequently newly confirmed PNe were carefully examined across the available HASH imagery compiled as part of the process of ingesting any new PN. These data also provided all the independently discovered PN central stars (CSPN) by looking for faint blue stars at/near the geometric centres of these new PNe. Even for large angular size PNe the CSPN is nearly always located at its exact centre (if visible in the available surveys) and is usually the only really blue star in the vicinity, giving confidence in its veracity. In Fig. 1 we give example images of one of the newly confirmed PNe ‘Ju 1’ (HASH ID 4408) that is $4'$ in diameter and its independently found CSPN. The left panel is a H α quotient image clearly showing the slightly oval PNe with the CSPN indicated by a red half-cross. The right panel gives a 2×2 arcminute RGB broad band image created from the ‘SSS’ (Hambly et al. 2001) i-band, r-band and B $_J$ band deep photographic data where the faint blue CSPN is clearly evident.

All candidates were observed as part of a long-term “filler” program with the OSIRIS long slit spectrograph on the Spanish 10.4 m Gran Telescopio Canarias (GTC) on La Palma in the Canary Islands. Such projects make decent use of time not suitable for the most challenging observing programs. This list is comprised of mainly large, very low surface brightness candidates not previously observed spectroscopically. It was supplemented by a further 16 PNe identified previously but that needed deeper spectroscopy for firmer confirmation. This provides a total of 78 GTC spectroscopic observations reported here. Of the 16 previously observed PNe candidates, one has been demoted as a result of these new observations from a ‘T’(True) to a ‘P’ (probable), IPHASX J023538.6+633823 has been upgraded from ‘P’ to ‘T’; IPHASX J055242.8+262116 from ‘L’ (Likely) to T and one, ‘Pa30’, is now known as a supernova remnant (SNR) of the historical Chinese guest star SN 1181 AD (Ritter et al. 2021). The other 12 remain as ‘T’ PNe.

The observations were performed between March 1st 2016 and May 17th 2018, under the programs GTC4-16AMEX, GTC12-17AMEX, GTC8-17BMEX and GTC11-18AMEX. Due to the constraints inherent to the filler mode, the observations were conducted under different seeing (up to $2''$), moon phase (dark to bright) and sky transparency (photometric to non-photometric) conditions. Such conditions are no serious impediment to the successful spectroscopic

follow-up of even very low surface brightness PNe that emit most of their light in narrow emission lines.

The spectroscopic data were obtained using two 2048×4096 Marconi CCD44-82 detectors with a pixel size of $15 \mu\text{m}/\text{pix}$. The plate scale was $0.254''$ per pixel with 2×2 binning adopted. We used the R1000B grating that provides long spectral coverage over the entire optical band from 3630\AA to 7500\AA , a dispersion of $2.12\text{\AA}/\text{pix}$ and a spectral resolution of 2.15\AA . Such a configuration allows detection of all significant optical emission lines from ionised plasmas, indispensable for the diagnostic identification and analysis of different kinds of nebulae, including PNe. The concurrent observation of spectrophotometric standard stars allowed flux calibration, necessary to determine the logarithmic extinction ($cH\beta$) from the corrected Balmer decrement. The chosen spectrograph setup also provides a resolving power sufficient to separate nearby diagnostic emission lines such as [S II] 6716\AA and [S II] 6731\AA used here for electronic density N_e estimates from the [SII] $6716 / 6731\text{\AA}$ line ratio (see later). The slit width was typically set to $0.8''$ (despite the variable seeing) to retain decent spectral resolution and the total exposure time ranged from 2000 to 3600 seconds depending on the surface brightness of the candidate nebulae.

In Table 1 we present summary data for the 55 discovered PN presented here and the 16 re-observations. The table lists, in order, the IAU PNG designation, PN usual name, HASH ID number, positional information (RA/DEC J2000 and Galactic latitude and longitude), PN status as T, L, P, whether there is a CSPN detected, the angular diameter in H α in arcseconds, the PN morphological classification following the ‘ERBIAS sparm’ scheme outlined in (Parker et al. 2006), the heliocentric radial velocity in km s^{-1} , slit position angle 0 for East to West, positive East towards South, negative East towards North), and exposure time.

3 DATA REDUCTION

Standard CCD spectrograph reduction steps were employed. These included combination of individual frames with cosmic ray rejection, bias subtraction, illumination correction, flat-fielding and wavelength calibration via standard calibration arc lamps. We used the IRAF based **GTCMOS pipeline** (Gómez-González et al. 2016) built for the purpose. The resulting 2-D images were then visually inspected to identify suitable sky and nebula extraction areas. This is given the extended nature of most of our PN candidates across the slit and in order to avoid contamination by stars. Any clearly identified PN central stars (CSPN), if falling on the slit, were extracted separately. The sky-subtracted, 1-D spectra of the PNe candidates were then co-added if necessary and subsequently flux calibrated to produce the final spectrum used for evaluation. An example flux-calibrated PN spectrum of Ju-1, first confirmed from these GTC data, is shown in Fig. 2 and displays the most common PN emission lines as marked.

4 DATA ANALYSIS

The first task was to use the observed spectral signatures and emission line ratios in an holistic combination with all other available imagery (including for object morphology and environment), object measurements and separate observations available conveniently in HASH, to make a decision on the true nature of the observed nebulae. This is following the robust precepts we have previously established, e.g. Frew & Parker, (2010) and Parker, (2022).

Of the 62 new PN candidates observed for this program we confirm

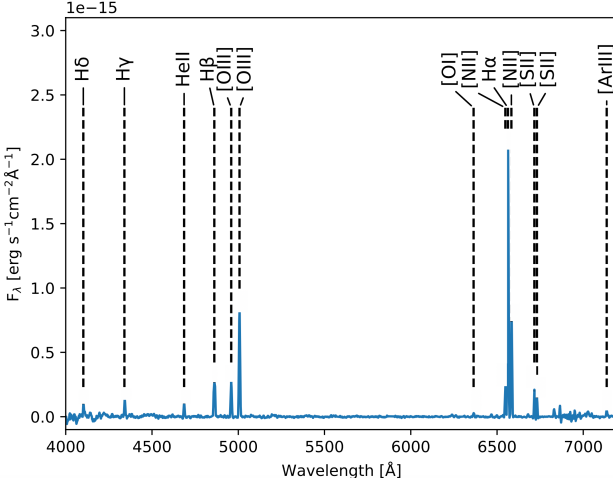


Figure 2. GTC spectrum of newly confirmed PN Ju-1 revealing a high excitation spectrum with prominent [OIII] 5007&4959Å H β , HeII 4686Å and H γ emission in the blue and H α , [NII], [SII] and [ArIII] lines in the red.

55, with 46 as True, 4 as Likely and 5 as Possible PNe. This gives a maximum confirmation rate of 89% with the remaining 7 rejected candidates being identified as a mixture of the various kinds of the usual PNe mimics (such as H II regions, parts of Supernova remnants and objects of unknown nature, but not PNe). These 7 rejected PNe and their GTC spectra can be examined, if required, via their unique HASH ID's as follows: 8241, 8248, 8448, 11583, 31955, 31956 and 31957.

4.1 Major axis diameters

A histogram of the major axis diameters in arcseconds ('') measured from the IPHAS H α imagery for the 55 new PNe confirmed here are presented in Fig. 3. Only 38% of the sample are less than 50'' in size with only 3 less than 10'' across while 34 (62%) have diameters >50''. The average diameter for the sample is 111'' with $\sigma = 107''$ confirming the wide angular size range but generally more extended nature of this sample. For comparison, the average angular diameter for all 2695 True PN in HASH, as at September 2022, is ~56''.

4.2 Spectral analysis

For the 55 new, confirmed PNe and for the 16 re-observed, spectral analysis was undertaken after first applying the standard heliocentric velocity correction in km s^{-1} . The spectral resolution employed is insufficient to determine useful kinematic information from the PNe, such as the PN shell's expansion velocity, but systemic velocities are reasonably well determined with typical velocity error of $\pm 15 \text{ km s}^{-1}$. We then fit all available emission lines above the background noise level in each spectrum with Gaussian profiles (recall there is little continuum in PNe spectra). Uncertainties were estimated by adding noise (the standard deviation of the spectrum around the emission lines) to the fitted profiles and re-fit 100 times. Using the Python package PyNeb developed by V. Luridiana, C. Morisset, and R.A. Shaw (Luridiana et al. 2015) we first calculated the reddening and corrected for it. We also simultaneously calculated nebula electron densities and, where possible, electron temperatures (given the principle diagnostic emission lines for the latter can be very weak). The emission

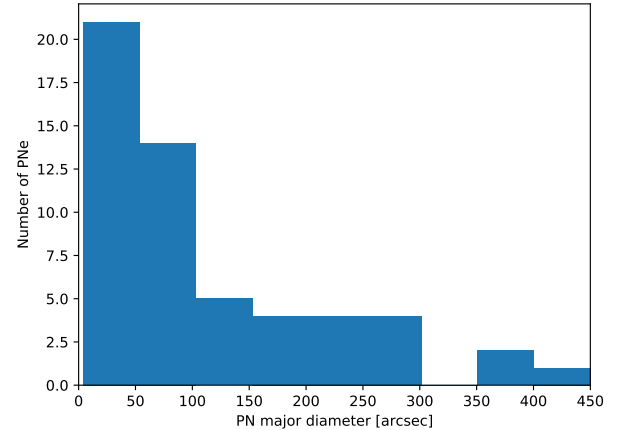


Figure 3. Histogram of major axis diameters in arcseconds for the 55 new PNe confirmed here. About 38% of the sample are less than 50'' in size but only 3 are less than 10'' across while 34 (62%) have diameters >50''.

line ratios are all used to self consistently determine such electron densities and temperatures as these variables are not independent but weakly correlated. This has been typically ignored in the past when determining electron densities for PNe by assuming a T_e of 10,000K.

To estimate the uncertainties of these physical characteristics we added 500 Monte-Carlo mock observations with the uncertainties from the line intensities to each spectrum. From this work, because of the limited S/N in many cases due to very low surface brightness and despite use of a 10 m-class telescope, only 27 objects (~ 39%, measured line intensities shown in Tab 2) out of combined total of 70 T,L,P PNe yielded both electron temperatures and densities from the diagnostic emission line ratios (this is from 55 new confirmations and 16 re-observations with 15 of these being confirmed). These PyNeb results are based on the usual [SII] 6717/6731 Å and [OII] 3737/3729 Å ratios traditionally used for plasma electron density estimates but accounting for electron temperature and then the usual [OIII] 4363/(5007+4959) Å or [NII] 5755/(6548+6583) Å ratios for electron temperature, while simultaneously accounting for density variations. Out of these 27 objects, 7 yielded the electron temperatures and densities from both sets of line ratios used to estimate these characteristics. The comparison of those 7 independently estimated values shows good agreement as can be seen for all the values given in Tab. 3.

In Fig. 4 we present the traditional ‘BPT’ diagnostic diagram (often used to separate different kinds of nebula source) (Baldwin et al. 1981) of all T,L,P PNe in this study following Frew & Parker (2010). In this particular example we plot emission line flux ratios of (H α)/[NII] versus $\log(\text{H}\alpha)/\text{[SII]}$, where [NII] refers to the sum of the fluxes of the two [NII] at 6548 and 6584 Å, and [SII] refers to the equivalent sum of the flux of the two [SII] lines at 6717 and 6731 Å. Nearly all points lie within the normal PNe range as indicated by the two black line tracks - see Fig.4 in (Frew & Parker 2010).

In Table 3 we present, where possible, estimates of the interstellar reddening E(B-V) and PN electron temperature and density determined from the measured flux calibrated emission lines as produced by PyNeb. Of the total PNe sample only 27 spectra had sufficiently high S/N to enable these measurements from detected lines.

4.3 Central stars and Gaia eDR3 distances

The identification of the Central Stars of PNe (CSPNe) is often difficult. They are generally faint and can be in a crowded field. While automated searches for CSPNe in GAIA have been devel-

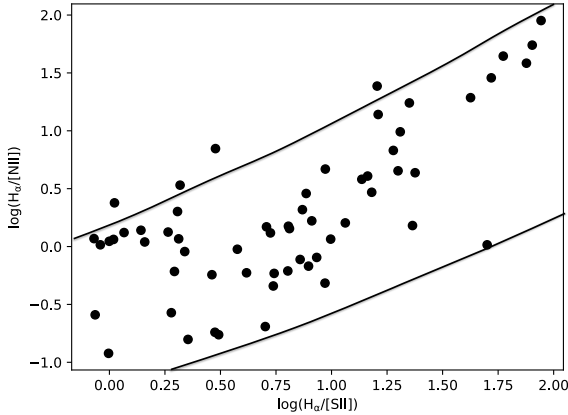


Figure 4. Standard $\log(\text{H}_\alpha)/[\text{NII}]$ versus $\log(\text{H}_\alpha)/[\text{SII}]$ ‘BPT’ diagnostic diagram for the confirmed PNe, where [NII] refers to the sum of the flux of the two red nitrogen lines at 6548 and 6584 Å, and [SII] refers to the equivalent sum of the flux of the two red sulphur lines at 6717 and 6731 Å. Nearly all points lie within the normal PNe range as indicated by the two black lines following the tracks in Fig.4 of (Frew & Parker 2010). A few points below $\log(\text{H}_\alpha)/[\text{SII}]$ of 0.5 and above $\log(\text{H}_\alpha)/[\text{NII}]$ of 0.0 overlap slightly with the typical SNR and Galactic HII locii.

oped (e.g. González-Santamaría et al. 2021; Chornay & Walton 2021; Parker et al. (2022) have shown that purely automated procedures can lead to miss-identifications. In fact 4 CSPNe reported in González-Santamaría et al. (2021) for PNGs 037.6-04.7, 059.2+01.0, 105.7+02.2, 149.1+08.7 are likely wrong, as well as 1 CSPN reported in Chornay & Walton (2021) (PNG 037.6-04.7). We therefore carefully inspected each PN for possible CSPN making use of the imagery conveniently provided by the HASH Database. For 36 new and 10 already known PN candidates (including Pa 30 which turned out to be a SNR and has subsequently been left out of the CSPNe analysis) a likely CSPN could be identified. Out of those 45 CSPNe, 41 could be identified in the GAIA DR3, with 38 (33 new, 5 already known PNe) having distances determined in Bailer-Jones et al. (2021). Only 1 CSPN has a radial velocity determined in GAIA DR3 (Gaia Collaboration et al. 2022, 2016). The Bailer-Jones et al. distances, GAIA DR3 radial velocities (where available), and the physical sizes (calculated from the geometric distances and HASH angular diameters) are shown in Tab. 4. A histogram of the physical sizes of the 38 PNe with distances is shown in Fig. 5.

5 CONCLUSIONS

We have spectroscopically confirmed 46 true, 4 likely, and 5 possible usually low surface brightness, generally large angular size PNe in the Northern Galactic plane for a total of 55 new PNe. These have now been incorporated into HASH together with their usually determined characteristics such as accurate position(s), morphology and angular size and presence of any CSPN. This PNe sample was effectively too difficult to confirm spectroscopically on smaller aperture telescopes. We have further refined the confidence and spectral characteristics for 16 previously observed PNe candidates, where the existing spectroscopy was too poor, and updated their HASH entries accordingly (with one being rejected as a PN). Seven new candidates observed were rejected as PNe based on our GTC spectroscopy. They remain in HASH as part of our large catalogue of various mimics. Where the PNe spectral S/N permits we have also calculated electron

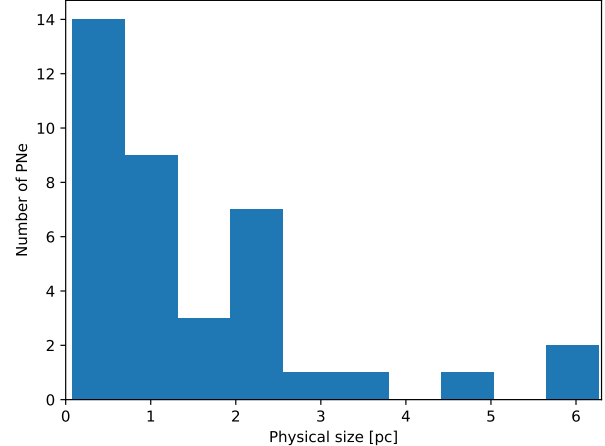


Figure 5. Physical sizes of the 38 PNe with Bailer-Jones et al. (2021) geometric distances, calculated from the HASH angular diameters.

temperatures and densities from either the [NII] / [SII] or the [OIII] / [SII] line ratios for 27 objects. We have also included estimates of interstellar reddening E(B-V) towards these PNe. We have found 37 of the 55 newly confirmed PNe to have credible blue CSPN identified from deep multi-wavelength images where PanSTARRS (Chambers et al. 2016) and SDSS (Gunn et al. 1998) imagery often play the key role. These CSPN co-ordinates have been added to HASH and cross checked against Gaia EDR3. This work has added about $\sim 2\%$ to the current total of confirmed Galactic PNe in HASH of over 3848 T,L,P entries.

ACKNOWLEDGEMENTS

QAP thanks the Hong Kong Research Grants Council for GRF research support under grants 17326116 and 17300417. AR thanks HKU for the provision of a postdoctoral fellowship. LS acknowledges support by UNAM PAPIIT project IN110122 (Mexico). This work has made use of data from the European Space Agency (ESA) mission *Gaia* (<https://www.cosmos.esa.int/gaia>), processed by the *Gaia* Data Processing and Analysis Consortium (DPAC, <https://www.cosmos.esa.int/web/gaia/dpac/consortium>). Funding for the DPAC has been provided by national institutions, in particular the institutions participating in the *Gaia* Multilateral Agreement.

6 DATA AVAILABILITY

The data underlying this article are available in the article itself and in its associated online material freely accessible from the HASH database found here: <http://hashpn.space> by simply entering the unique HASH ID number for each source as provided.

Table 1: Summary of key data for the 55 newly confirmed PNe including ID, HASH ID, position (RA/DEC J2000 and Galactic l/b), T,L,P status, whether there is a CSPN detected, angular size, Morphology, heliocentric spectroscopic radial velocity, slit position angle (0 for East to West, positive East towards South, negative East towards North), and the exposure time (if observed in more than one night then the exposure times are added together). The last 16 entries in the table are for previously observed candidates that required better spectra for final confirmation. 'IX' stands for 'IPHASX'.

IAU PNG	Target Name	HASH ID	RA	DEC	l	b	Status	CS	Ang. Diam. ["]	Morphology	v _{rad} [km s ⁻¹]	PA [°]	t _{exp} [s]
037.6-04.7	BMP J1917+0200	2502	19:17:07.30	02:00:10.15	37.6558	-4.7916	T	y	76x64	Ea	33.8	-90	2*1200
037.9-03.4	Abell 56	390	19:13:06.10	02:52:47.89	37.9727	-3.4965	T	y	206x182	Rmr	-3.2	73	2*1000 + 2*1000
038.7-02.4	IX J191058.9+040350	8193	19:10:58.90	04:03:50.40	38.7811	-2.4816	T	n	11	Ba	19.6	0	2*1200
040.5-00.0	IX J190543.8+064413	8190	19:05:43.80	06:44:13.34	40.5534	-0.0911	T	n	14	Ea	77.6	-90	2*1000
040.6-01.5	IRAS 19086+0603	8528	19:11:04.80	06:08:45.06	40.6406	-1.5428	T	n	32x22	Bam	89.5	-43	2*1000
043.8+02.1	IXJ190333	8506	19:03:38.50	10:42:27.47	43.8464	2.1878	P	n	450	A	41.1	54	
051.3+01.8	PM 1-295	452	19:19:18.80	17:11:48.08	51.3613	1.8143	L	y	20	Rm	-19.2	-90	2*1000
057.6+01.8	PM 1-305	4819	19:31:41.30	22:43:38.75	57.6121	1.8763	T	y	15	Eas	11.8	19	30
058.1-00.8	IX J194301.3+215424	8566	19:43:01.30	21:54:24.91	58.1786	-0.8113	T	n	14	B	17.8	-45	2*1250 + 2*1250
058.9+09.0	Si 1-2	486	19:06:07.20	27:12:58.50	58.9398	9.0837	T	y	60	Ra	33.8	11	2*1300
059.2+01.0	Ou 3	10957	19:38:17.54	23:45:48.70	59.255	1.0531	T	y	90	Rar	-12.8	17	2*1250
060.0-04.3	Abell 68	495	20:00:10.60	21:42:56.02	60.0457	-4.3343	T	y	38	Bas	-20.1	-25	2*1000
060.5+05.6	Pa 21	15561	19:23:15.00	27:07:34.36	60.5899	5.6419	T	n	4x2	S	-23.8	-20	2*1250
062.1+03.1	IX J193617.5+272051	8206	19:36:17.61	27:20:51.90	62.1658	3.1954	T	y	9	Ra	-82.3	14	2*1250
062.4+00.6	IX J194645.3+262211	8214	19:46:45.30	26:22:11.50	62.4691	0.6838	P	n	290	A	14.6	14	2*1200
062.5-01.8	IX J195627.3+250648	8219	19:56:27.30	25:06:48.56	62.5056	-1.8359	L	n	24	E	20.5	-19	2*1300
063.1+00.8	IX J194745.5+270150	8217	19:47:45.50	27:01:50.70	63.1529	0.8232	P	n	207	Ea	-35.2	12	2*1300
064.9-09.1a	Pa 15	15551	20:29:07.63	23:11:09.30	64.9665	-9.1329	T	y	12	Ers	-1.9	-26	2*500
066.1+04.7	IX J193849.6+313744	8210	19:38:49.70	31:37:44.83	66.1861	4.7925	T	y	160	Ear	-9.2	-3	2*1300
066.5-14.8	Kn 45	4359	20:53:03.94	21:00:10.90	66.5074	-14.8979	T	y	145x138	Ears	-53.9	26	2*1200
066.9-07.8	Kn 19	4356	20:29:20.60	25:32:39.84	66.9484	-7.8206	T	y	74x73	Rars	15.5	14	2*1200
067.3-02.6	IX J201058.0+284455	8232	20:10:58.00	28:44:55.00	67.3074	-2.6396	T	n	48x36	Bap	29.2	-6	2*1300
069.6-03.7	Kn 20	10881	20:21:26.47	30:05:38.01	69.6977	-3.7869	T	n	16	Rr	26.4	-10	2*1250
070.5+11.0	Kn 61	10899	19:21:38.94	38:18:57.20	70.524	11.0068	T	y	100x92	Rrs	-21.5	-6	2*1300
073.4+01.5	IRAS 20084+3604	8230	20:10:17.90	36:13:09.73	73.4897	1.5595	P	n	13.9	Eam	-88.2	31	2*1250
075.0-07.2	Pa 27	15564	20:48:58.37	32:18:14.80	75	-7.2043	T	y	72x60	Eam	-24.7	15	3*800
075.3+05.5	Pa 22	15565	19:58:13.08	39:54:40.80	75.3581	5.5347	T	y	49x45	Eas	-33.4	46	2*1250
075.5+01.7	Ju 1	4408	20:15:21.45	38:02:43.80	75.5701	1.7233	T	y	240	Rr	31.5	67	2*1200
076.8-08.1	Pa 28	15566	20:58:10.94	33:08:33.10	76.8932	-8.1711	T	y	133x123	Ears	10.5	-3	2*1300
078.4-07.2	Pa 29	15567	20:59:43.50	34:54:23.00	78.4594	-7.2741	T	y	4	E	-194.6	-18	30
079.8-10.2	Alves 1	10960	21:15:06.60	33:58:18.01	79.8888	-10.2639	T	y	270	Es	21.4	-2	2*1300
082.1-07.8	Kn 24	560	21:13:37.70	37:15:37.44	82.1173	-7.8014	T	y	190	Bams	-6.0	34	2*1300 + 2*1000
082.5-06.2	Kn 25	4362	21:09:20.20	38:36:06.12	82.5312	-6.2696	T	y	79x57	Bmp	-17.9	-80	2*1200
093.8-00.2	LDu 18	17066	21:29:52.30	50:54:21.64	93.8654	-0.2238	T	n	21	Rar	-51.7	-151	2*1250
094.5-00.8a	LDu 1	10959	21:36:05.80	50:54:09.29	94.5844	-0.8915	T	y	132x120	Rars	-36.6	-45	2*1300 + 2*1000
098.3-04.9	Pa 41	15568	22:10:13.64	50:04:33.40	98.3084	-4.928	T	y	102x82	Ea	-48.0	5	2*1300
099.1+05.7	KTC 1	4367	21:28:11.00	58:52:34.68	99.1885	5.7209	T	y	22x16	E	-50.8	62	300
099.7-08.8	HaWe 15	602	22:30:33.43	47:31:23.30	99.7159	-8.8978	T	y	295x180	Em	-3.7	14	2*1300
103.7+07.2	Kn 30	4368	21:47:24.50	63:05:09.60	103.766	7.2839	T	y	13x12	Eamrs	-130.2	-44	2*1250
107.0+21.3	K 1-6	617	20:04:14.28	74:25:36.00	107.0357	21.3839	T	n	198x160	Ea	-6.0	-78	2*1200
111.2-03.0	We 2-260	8266	23:22:23.70	57:46:27.98	111.2606	-3.0654	T	n	162x132	Bams	-15.6	26	1600 + 2*1300
120.4-01.3	Ou 2	10956	00:30:56.74	61:24:34.30	120.4821	-1.3647	T	y	76	Emrs	-98.7	78	2*1200 + 2*1300

Table 1: Summary of key data for the 55 newly confirmed PNe including ID, HASH ID, position (RA/DEC J2000 and Galactic l/b), T,L,P status, whether there is a CSPN detected, angular size, Morphology, heliocentric spectroscopic radial velocity, slit position angle (0 for East to West, positive East towards South, negative East towards North), and the exposure time (if observed in more than one night then the exposure times are added together). The last 16 entries in the table are for previously observed candidates that required better spectra for final confirmation. 'IX' stands for 'IPHASX'.

IAU PNG	Target Name	HASH ID	RA	DEC	l	b	Status	CS	Ang. Diam. ["]	Morphology	$v_{\text{rad}} [\text{km s}^{-1}]$	PA [$^{\circ}$]	$t_{\text{exp}} [\text{s}]$
129.2-02.0	We 2-5	655	01:42:37.88	60:09:47.20	129.2637	-2.0778	T	y	210x165	Bamrs	-33.4	45	2*1000 + 2*1250
129.6-05.6	KLSS 2-8	658	01:40:05.84	56:34:54.60	129.6292	-5.6559	T	y	90x75	Er	-97.3	80	2*1300
136.8-13.2	Kn 58	10896	02:12:27.84	47:27:10.10	136.8472	-13.2179	T	y	75x52	B	-133.4	-90	2*1250
138.1+04.1	Sh 2-200	670	03:10:58.86	62:47:54.90	138.128	4.1193	T	n	360x345	Eamrs	-48.9	52	2*1000
139.3+04.8	KK 26	4393	03:23:04.90	62:47:11.76	139.311	4.8418	T	n	106x54	Bams	-3.7	-18	2*1200
147.1-09.0	HaWe 3	4495	03:16:34.00	46:53:37.39	147.1045	-9.0531	T	y	38x36	Ears	-5.5	2	2*30
147.2+08.3	Kn 33	4330	04:32:38.10	60:20:12.12	147.2155	8.365	T	y	17x16	Ras	41.5	24	30
151.0-00.4	Ou 1	8458	04:07:21.58	51:24:22.40	151.009	-0.457	L	y	95x75	I	-1.4	0	2*1000
154.8+05.9	Kn 36	4333	04:55:24.50	52:59:15.00	154.8942	5.9869	T	n	59x50	Ear	15.5	21	1800
164.8-09.8	Kn 51	10890	04:25:26.86	35:06:07.80	164.806	-9.8386	T	y	84x60	Iams	32.8	-8	2*1300
174.6-05.2	IX J051152.2+302751	8313	05:11:52.20	30:27:51.19	174.6695	-5.2616	P	y	375x245	Er	1.8	0	2*1200
175.6+11.4	Kn 62	15571	06:23:55.42	38:15:14.50	175.6316	11.4563	T	y	126	R	88.6	3	2*1300
182.3-03.7	IX J053650.8+245616	8331	05:36:50.80	24:56:16.69	182.364	-3.7717	L	n	300x225	B	-8.3	-43	2*1500
040.7+03.4	IX J185322.1+083018	4424	18:53:22.10	08:30:18.00	40.7292	3.4413	T	n	110	Rar	-45.3	-40	2*1500
059.1-01.4	Ra 17	8215	19:47:28.90	22:28:23.81	59.1857	-1.4214	T	y	27	Ras	-13.3	18	2*1300
060.2+00.8	Kn 11	10878	19:41:19.10	24:30:52.56	60.2489	0.8219	T	n	9	B	-11.0	-17	1000
086.1+05.4	We 1-10	571	20:31:52.36	48:52:49.70	86.1906	5.4601	T	y	195x185	Rar	-3.2	11	2*1000
086.9-03.4	Ou 5	15806	21:14:20.03	43:41:36.00	86.9108	-3.4821	T	y	33x20	Bmp	-38.0	-14	2*1000
095.1+00.9	KKR 62	4431	21:30:44.90	52:41:48.84	95.1902	0.9889	T	n	56x45	B	-3.7	73	2*1250
095.2+25.4	Kn 59	10897	18:41:41.90	65:11:57.98	95.2776	25.4542	T	y	4	Ramrs	4.5	-88	2*900
097.4+12.3	KnFe 1	10889	20:38:09.19	61:55:02.90	97.425	12.3683	T	y	42x36	Ers	-18.8	65	2*1200
098.9+03.0	IX J214032.5+564751	10285	21:40:32.60	56:47:51.61	98.9933	3.0779	T	n	9.4	Rr	-64.9	-59	2*540
100.3+02.8	Cr 1	4386	21:49:11.69	57:27:19.70	100.3154	2.8183	P	n	120x106	Es	-43.9	-16	2*1250
105.7+02.2	FsMv 1	5240	22:25:56.90	60:11:48.12	105.7755	2.2642	T	y	88	Eas	-82.3	54	2*1300
109.4+07.7	Kn 31	4369	22:27:39.19	66:44:09.50	109.4006	7.72	T	y	80	Rars	-31.6	56	2*1300
123.0+04.6	Pa 30	15569	00:53:11.20	67:30:02.40	123.0998	4.6295	SNR	y	171x156		9.1	-60	2*1300
134.1+03.0	IX J023538.6+633823	4425	02:35:39.40	63:38:23.93	134.1943	3.0706	T	n	135	Ea	-7.4	-64	2*1300
149.1+08.7	Kn 34	4332	04:45:18.65	59:09:24.60	149.1755	8.7933	T	y	60x57	Rars	51.1	20	2*1200
183.0+00.0	IX J055242.8+262116	9824	05:52:42.80	26:21:16.09	183.02190	0.01762	T	y	16.1	Ramr	76.7	-43	4*750

Table 2: Line intensities for each PN from the 27 PNe spectra with sufficient S/N of which 23 are for the new PNe discovered. "n.d." stands for not detected.

IAU PNG	H_{α}	H_{β}	[NII] 5755Å	[NII] 6548Å	[NII] 6584Å	[OIII] 4363Å	[OIII] 5007Å	[SII] 6716Å	[SII] 6731Å
037.6-04.7	$1.3e-15 \pm 8.3e-18$	$3.0e-16 \pm 7.7e-18$	$2.8e-17 \pm 9.6e-18$	$5.6e-16 \pm 6.8e-18$	$1.8e-15 \pm 7.2e-18$	n.d.	$4.1e-16 \pm 6.7e-18$	$2.6e-16 \pm 7.6e-18$	$2.0e-16 \pm 8.0e-18$
037.9-03.4	$7.2e-15 \pm 1.1e-16$	$1.6e-15 \pm 7.5e-17$	$2.5e-16 \pm 8.3e-17$	$8.9e-15 \pm 1.2e-16$	$2.6e-14 \pm 1.2e-16$	n.d.	$2.7e-15 \pm 6.8e-17$	$9.5e-16 \pm 1.0e-16$	$4.7e-16 \pm 1.1e-16$
040.6-01.5	$2.9e-15 \pm 5.6e-18$	$8.5e-17 \pm 4.7e-18$	$1.8e-17 \pm 3.3e-18$	$2.6e-15 \pm 5.3e-18$	$8.3e-15 \pm 5.6e-18$	n.d.	$5.8e-16 \pm 4.0e-18$	$8.2e-16 \pm 5.2e-18$	$7.1e-16 \pm 5.3e-18$
057.6+01.8	$9.8e-14 \pm 4.2e-17$	$1.0e-14 \pm 3.8e-17$	n.d.	$8.5e-16 \pm 4.6e-17$	$1.7e-15 \pm 3.9e-17$	$6.9e-16 \pm 6.0e-17$	$8.6e-14 \pm 3.8e-17$	$6.2e-16 \pm 4.3e-17$	$6.8e-16 \pm 3.7e-17$
058.9+09.0	$1.6e-14 \pm 3.3e-17$	$4.7e-15 \pm 1.0e-16$	$7.1e-17 \pm 3.9e-17$	$2.8e-15 \pm 3.1e-17$	$9.0e-15 \pm 3.2e-17$	n.d.	$3.5e-14 \pm 9.1e-17$	$1.6e-15 \pm 2.8e-17$	$1.3e-15 \pm 2.9e-17$
059.1-01.4	$2.2e-15 \pm 1.5e-17$	$3.6e-16 \pm 4.8e-17$	$8.2e-17 \pm 1.5e-17$	$5.1e-16 \pm 1.7e-17$	$1.4e-15 \pm 1.5e-17$	n.d.	$1.6e-15 \pm 3.7e-17$	$1.3e-15 \pm 1.3e-17$	$8.6e-16 \pm 1.5e-17$
060.0-04.3	$5.4e-14 \pm 3.1e-17$	$1.2e-14 \pm 3.3e-17$	n.d.	$3.2e-15 \pm 2.8e-17$	$8.8e-15 \pm 2.8e-17$	$3.5e-16 \pm 5.3e-17$	$5.8e-14 \pm 3.7e-17$	$1.6e-15 \pm 3.0e-17$	$1.1e-15 \pm 2.5e-17$
060.5+05.6	$9.3e-16 \pm 4.5e-18$	$1.3e-16 \pm 7.6e-18$	$1.7e-17 \pm 6.4e-18$	$2.7e-16 \pm 4.5e-18$	$8.8e-16 \pm 4.4e-18$	n.d.	$2.7e-15 \pm 7.6e-18$	$4.0e-17 \pm 3.9e-18$	$6.8e-17 \pm 4.3e-18$
069.6-03.7	$4.0e-15 \pm 9.7e-18$	$5.1e-16 \pm 2.9e-17$	$5.5e-17 \pm 1.5e-17$	$6.0e-16 \pm 1.1e-17$	$1.8e-15 \pm 1.1e-17$	n.d.	$4.2e-15 \pm 2.3e-17$	$2.7e-16 \pm 8.5e-18$	$2.1e-16 \pm 7.8e-18$
073.4+01.5	$1.1e-15 \pm 3.5e-18$	$1.1e-18 \pm 1.2e-18$	$7.0e-18 \pm 3.1e-18$	$1.3e-16 \pm 3.3e-18$	$4.1e-16 \pm 3.5e-18$	n.d.	$2.9e-16 \pm 3.6e-18$	$2.4e-16 \pm 3.2e-18$	
075.3+05.5	$1.5e-15 \pm 5.6e-18$	$5.1e-16 \pm 9.4e-18$	n.d.	$3.0e-17 \pm 6.7e-18$	$5.6e-17 \pm 5.8e-18$	$4.9e-17 \pm 1.5e-17$	$3.2e-15 \pm 7.8e-18$	$3.0e-17 \pm 1.1e-17$	$3.6e-17 \pm 1.1e-17$
078.4-07.2	$3.8e-15 \pm 4.6e-18$	$1.1e-15 \pm 9.4e-18$	n.d.	$1.4e-17 \pm 4.1e-18$	$2.8e-17 \pm 3.7e-18$	$7.8e-17 \pm 1.7e-17$	$3.8e-15 \pm 9.9e-18$	$1.8e-17 \pm 6.4e-18$	$2.6e-17 \pm 6.4e-18$
082.5-06.2	$2.1e-15 \pm 1.1e-17$	$5.8e-16 \pm 1.9e-17$	n.d.	$1.9e-16 \pm 1.1e-17$	$5.3e-16 \pm 1.0e-17$	$5.4e-17 \pm 2.9e-17$	$5.0e-15 \pm 1.8e-17$	$9.5e-17 \pm 1.1e-17$	$4.6e-17 \pm 9.1e-18$
086.9-03.4	$4.6e-14 \pm 1.5e-17$	$6.9e-15 \pm 3.2e-17$	$3.1e-17 \pm 1.5e-17$	$5.9e-16 \pm 1.5e-17$	$1.8e-15 \pm 1.6e-17$	$2.5e-16 \pm 6.3e-17$	$3.9e-14 \pm 2.7e-17$	$6.2e-16 \pm 1.8e-17$	$4.6e-16 \pm 1.7e-17$
095.1+00.9	$7.0e-15 \pm 2.5e-17$	$6.2e-16 \pm 4.0e-17$	$6.4e-17 \pm 2.6e-17$	$2.8e-15 \pm 2.3e-17$	$8.5e-15 \pm 2.3e-17$	n.d.	$5.7e-15 \pm 4.0e-17$	$6.3e-16 \pm 2.1e-17$	$4.7e-16 \pm 2.3e-17$
095.2+25.4	$1.0e-14 \pm 1.3e-17$	$3.5e-15 \pm 1.2e-17$	$8.8e-17 \pm 1.1e-17$	$2.8e-15 \pm 1.5e-17$	$8.3e-15 \pm 1.4e-17$	$7.5e-17 \pm 2.7e-17$	$2.5e-15 \pm 1.1e-17$	$2.6e-15 \pm 1.2e-17$	$2.0e-15 \pm 1.4e-17$
097.4+12.3	$4.4e-15 \pm 9.5e-18$	$1.3e-15 \pm 8.2e-18$	$1.7e-17 \pm 1.0e-17$	$2.9e-16 \pm 1.0e-17$	$8.6e-16 \pm 9.1e-18$	$1.7e-16 \pm 1.8e-17$	$1.2e-14 \pm 8.9e-18$	$1.9e-16 \pm 8.8e-18$	$1.3e-16 \pm 9.0e-18$
098.9+03.0	$3.4e-15 \pm 1.4e-17$	$4.5e-16 \pm 3.6e-17$	$5.7e-17 \pm 1.2e-17$	$7.6e-16 \pm 1.5e-17$	$2.1e-15 \pm 1.7e-17$	$1.5e-16 \pm 5.0e-17$	$3.6e-15 \pm 3.2e-17$	$1.8e-16 \pm 1.6e-17$	$1.6e-16 \pm 1.5e-17$
099.7-08.8	$1.3e-14 \pm 5.8e-17$	$4.0e-15 \pm 4.0e-17$	$1.4e-16 \pm 5.7e-17$	$4.2e-15 \pm 5.4e-17$	$1.3e-14 \pm 5.1e-17$	$2.9e-16 \pm 8.2e-17$	$2.2e-14 \pm 3.8e-17$	$1.1e-15 \pm 5.2e-17$	$6.6e-16 \pm 4.8e-17$
111.2-03.0	$2.2e-15 \pm 8.4e-17$	$2.2e-18 \pm 1.5e-92$	$2.4e-16 \pm 8.2e-17$	$4.8e-15 \pm 1.1e-16$	$1.4e-14 \pm 8.3e-17$	n.d.	$1.8e-15 \pm 7.9e-17$	$1.3e-15 \pm 7.5e-17$	$1.0e-15 \pm 7.7e-17$
120.4-01.3	$4.4e-15 \pm 1.2e-17$	$8.4e-16 \pm 1.5e-17$	n.d.	$1.3e-16 \pm 1.1e-17$	$3.3e-16 \pm 1.0e-17$	$1.2e-16 \pm 2.2e-17$	$1.0e-14 \pm 1.4e-17$	$1.2e-16 \pm 1.1e-17$	$9.9e-17 \pm 1.1e-17$
129.2-02.0	$7.1e-15 \pm 6.0e-17$	$1.5e-15 \pm 3.0e-18$	$2.2e-16 \pm 3.6e-17$	$1.0e-14 \pm 4.7e-17$	$3.1e-14 \pm 5.1e-17$	n.d.	$2.2e-15 \pm 9.2e-18$	$1.3e-15 \pm 4.6e-17$	$9.6e-16 \pm 5.4e-17$
136.8-13.2	$2.0e-14 \pm 3.6e-17$	$6.3e-15 \pm 8.3e-17$	n.d.	$6.9e-16 \pm 3.9e-17$	$7.4e-16 \pm 1.6e-16$	$5.5e-14 \pm 7.2e-17$	$2.2e-16 \pm 3.3e-17$	$1.6e-16 \pm 3.2e-17$	
139.3+04.8	$3.1e-14 \pm 3.7e-17$	$4.3e-15 \pm 4.1e-17$	$1.2e-16 \pm 2.7e-17$	$5.1e-15 \pm 3.8e-17$	$1.6e-14 \pm 3.6e-17$	$3.3e-16 \pm 7.2e-17$	$5.1e-14 \pm 3.3e-17$	$2.8e-15 \pm 3.9e-17$	$2.1e-15 \pm 4.5e-17$
147.2+08.3	$2.5e-14 \pm 1.7e-17$	$5.0e-15 \pm 3.8e-18$	$1.6e-16 \pm 1.8e-17$	$4.4e-15 \pm 1.6e-17$	$1.3e-14 \pm 1.8e-17$	$1.7e-16 \pm 3.3e-17$	$1.3e-14 \pm 3.9e-18$	$9.7e-15 \pm 1.6e-17$	$8.0e-15 \pm 1.7e-17$
151.0-00.4	$6.9e-15 \pm 1.9e-17$	$1.8e-15 \pm 2.0e-17$	$6.1e-17 \pm 1.6e-17$	$1.5e-15 \pm 1.9e-17$	$4.5e-15 \pm 2.0e-17$	n.d.	$7.9e-15 \pm 1.9e-17$	$2.0e-15 \pm 1.5e-17$	$1.4e-15 \pm 1.6e-17$
182.3-03.7	$1.5e-15 \pm 3.6e-17$	$1.9e-16 \pm 6.4e-17$	$1.0e-16 \pm 3.6e-17$	$1.1e-16 \pm 3.8e-17$	$5.1e-16 \pm 3.4e-17$	n.d.	$1.3e-15 \pm 6.3e-17$	$8.5e-16 \pm 3.6e-17$	$5.8e-16 \pm 3.5e-17$

Table 3: Estimates of the Interstellar reddening E(B-V) and nebula electron temperature and density from the 27 PNe spectra with sufficient S/N of which 23 are for the new PNe discovered. Note the large errors on many measures.

IAU PNG	E(B-V)	$T_{e^-}([NII], [SII])[K]$	$T_{e^-}([OIII], [SII])[K]$	$\rho_{e^-}([NII], [SII])[\text{cm}^{-3}]$	$\rho_{e^-}([OIII], [SII])[\text{cm}^{-3}]$
037.6-04.7	0.391 ± 0.018	11093 ± 2246		159 ± 70	
037.9-03.4	0.373 ± 0.030	8603 ± 1346		101 ± 84	
040.6-01.5	2.145 ± 0.047	7220 ± 475		306 ± 16	
057.6+01.8	1.049 ± 0.003		13180 ± 355		1124 ± 169
058.9+09.0	0.129 ± 0.015	8580 ± 1927		151 ± 34	
059.1-01.4	0.676 ± 0.097	32334 ± 9084		7 ± 5	
060.0-04.3	0.419 ± 0.002		10487 ± 508		18 ± 12
060.5+05.6	0.793 ± 0.045	12796 ± 2644		5921 ± 4999	
069.6-03.7	0.860 ± 0.037	18620 ± 4348		166 ± 85	
073.4+01.5	5.067 ± 0.791	49961 ± 23354		344 ± 86	
075.3+05.5	0.022 ± 0.014		13365 ± 1927		3136 ± 5360
078.4-07.2	0.187 ± 0.010		15836 ± 1652		5141 ± 6731
082.5-06.2	0.226 ± 0.027		13228 ± 1089		108 ± 120
086.9-03.4	0.723 ± 0.003	12817 ± 3837	11351 ± 855	90 ± 11	92 ± 10
095.1+00.9	1.182 ± 0.048	9370 ± 1647		110 ± 57	
095.2+25.4	0.002 ± 0.002	8770 ± 1128	17976 ± 3975	204 ± 12	240 ± 17
097.4+12.3	0.161 ± 0.006	11809 ± 3480	13689 ± 668	73 ± 57	80 ± 63
098.9+03.0	0.820 ± 0.064	16044 ± 2598	21227 ± 2873	431 ± 255	491 ± 293
099.7-08.8	0.121 ± 0.008	7526 ± 1043	13089 ± 460	17 ± 14	16 ± 0
111.2-03.0	5.053 ± 0.033	51714 ± 23756		363 ± 293	
120.4-01.3	0.524 ± 0.014		13600 ± 1066		446 ± 306
129.2-02.0	0.436 ± 0.008	8213 ± 491		110 ± 67	
136.8-13.2	0.090 ± 0.012		12945 ± 1117		365 ± 381
139.3+04.8	0.805 ± 0.005	8859 ± 1028	11503 ± 850	95 ± 32	97 ± 35
147.2+08.3	0.465 ± 0.000	10112 ± 649	14359 ± 1198	262 ± 5	287 ± 6
151.0-00.4	0.276 ± 0.004	10206 ± 2104		62 ± 17	
182.3-03.7	0.950 ± 0.304	44981 ± 24900		99 ± 50	

Table 4: Central stars with [Bailer-Jones et al. \(2021\)](#) distances, physical diameters from HASH angular diameters and r_{geo} , and GAIA DR3 radial velocities (where available).

IAU PNG	HASH ID	GAIA ID	r_{geo} [pc]	r_{phot} [pc]	physical diameter [pc]	v_{rad} [km s $^{-1}$]
037.9-03.4	390	4268179207028750592	4836^{+3985}_{-2300}	1081^{+316}_{-228}	$4.830^{+3.980}_{-2.297} \times 4.268^{+3.516}_{-2.029}$	-
051.3+01.8	452	4514868732516293760	2230^{+102}_{-87}	2254^{+152}_{-112}	$0.216^{+0.010}_{-0.008} \times 0.216^{+0.010}_{-0.008}$	-
057.6+01.8	4819	2019351991760108672	3326^{+1606}_{-1281}	6727^{+2418}_{-1671}	$0.242^{+0.117}_{-0.093} \times 0.242^{+0.117}_{-0.093}$	-
058.9+09.0	486	2036937138334923648	2633^{+1258}_{-857}	2201^{+1375}_{-809}	$0.766^{+0.366}_{-0.249} \times 0.766^{+0.366}_{-0.249}$	-
059.2+01.0	10957	2020279846433107200	2948^{+2911}_{-1302}	11210^{+2509}_{-1690}	$1.287^{+1.270}_{-0.568} \times 1.287^{+1.270}_{-0.568}$	-
060.0-04.3	495	1826936121144576896	2844^{+1514}_{-931}	12300^{+1296}_{-1178}	$0.524^{+0.279}_{-0.172} \times 0.524^{+0.279}_{-0.172}$	-
062.1+03.1	8206	2025166763313254400	7091^{+4254}_{-3595}	26909^{+6721}_{-3839}	$0.309^{+0.186}_{-0.157} \times 0.309^{+0.186}_{-0.157}$	-
064.9-09.1a	15551	1830887113098897920	3961^{+1098}_{-804}	3949^{+1598}_{-982}	$0.230^{+0.064}_{-0.047} \times 0.230^{+0.064}_{-0.047}$	-
066.1+04.7	8210	2033203609193896064	7477^{+3235}_{-2852}	21607^{+3845}_{-13178}	$5.800^{+2.510}_{-2.212} \times 5.800^{+2.510}_{-2.212}$	-
066.5-14.8	4359	1814597642173959168	2819^{+1722}_{-1023}	1060^{+81}_{-77}	$1.982^{+1.211}_{-0.719} \times 1.886^{+1.152}_{-0.685}$	-
066.9-07.8	4356	1832550223218972800	5567^{+2741}_{-2137}	4957^{+2748}_{-2150}	$1.997^{+0.984}_{-0.767} \times 1.970^{+0.970}_{-0.756}$	-
070.5+11.0	10899	2052811676760671872	5882^{+2441}_{-1775}	4195^{+1936}_{-1393}	$2.852^{+1.183}_{-0.861} \times 2.624^{+1.089}_{-0.792}$	-
075.0-07.2	15564	1859955657931121536	1436^{+23}_{-24}	1430^{+27}_{-26}	$0.501^{+0.008}_{-0.008} \times 0.418^{+0.007}_{-0.007}$	-47.4 ± 2.3
075.3+05.5	15565	2072773550888053888	7103^{+2837}_{-2086}	22112^{+3220}_{-3585}	$1.687^{+0.674}_{-0.496} \times 1.550^{+0.619}_{-0.455}$	-
075.5+01.7	4408	2060926897208561280	1426^{+741}_{-386}	1767^{+1416}_{-884}	$1.659^{+0.862}_{-0.449} \times 1.659^{+0.862}_{-0.449}$	-
076.8-08.1	15566	1865874672618774656	3881^{+1459}_{-1161}	2355^{+512}_{-397}	$2.503^{+0.941}_{-0.749} \times 2.315^{+0.870}_{-0.692}$	-
078.4-07.2	15567	1866682878077985920	4373^{+2464}_{-1880}	1979^{+3729}_{-1410}	$0.085^{+0.048}_{-0.036} \times 0.085^{+0.048}_{-0.036}$	-
079.8-10.2	10960	1866922365452368768	1903^{+600}_{-371}	1099^{+919}_{-105}	$2.492^{+0.785}_{-0.486} \times 2.492^{+0.785}_{-0.486}$	-
082.1-07.8	560	1868658082001121664	2567^{+996}_{-861}	1742^{+233}_{-238}	$2.365^{+0.917}_{-0.793} \times 2.365^{+0.917}_{-0.793}$	-
098.3-04.9	15568	1976783887984709120	2199^{+320}_{-265}	2284^{+423}_{-292}	$1.088^{+0.158}_{-0.131} \times 0.874^{+0.127}_{-0.105}$	-
099.1+05.7	4367	2179544655458448512	4854^{+1228}_{-1072}	4037^{+767}_{-699}	$0.518^{+0.131}_{-0.114} \times 0.377^{+0.095}_{-0.083}$	-
099.7-08.8	602	1986574557983855104	1302^{+224}_{-143}	1093^{+113}_{-111}	$1.863^{+0.320}_{-0.205} \times 1.137^{+0.195}_{-0.125}$	-
103.7+07.2	4368	2216463232261024896	5845^{+6396}_{-2553}	6513^{+1207}_{-2129}	$0.368^{+0.403}_{-0.161} \times 0.340^{+0.372}_{-0.149}$	-
120.4-01.3	10956	430204780732841600	1586^{+823}_{-378}	1901^{+1675}_{-757}	$0.584^{+0.303}_{-0.139} \times 0.584^{+0.303}_{-0.139}$	-
129.2-02.0	655	509636112062310016	3429^{+1599}_{-1398}	2837^{+992}_{-845}	$3.492^{+1.628}_{-1.423} \times 2.743^{+1.279}_{-1.118}$	-
129.6-05.6	658	409721566300550656	1187^{+789}_{-340}	871^{+601}_{-410}	$0.518^{+0.344}_{-0.148} \times 0.432^{+0.287}_{-0.124}$	-
136.8-13.2	10896	354941216942517504	2843^{+2130}_{-1084}	1386^{+45}_{-338}	$1.034^{+0.775}_{-0.394} \times 0.717^{+0.537}_{-0.273}$	-
147.1-09.0	4495	434853485833190528	4089^{+1470}_{-955}	3633^{+843}_{-556}	$0.753^{+0.271}_{-0.176} \times 0.714^{+0.257}_{-0.167}$	-
147.2+08.3	4330	471551198232719744	2393^{+2979}_{-1243}	1326^{+1629}_{-454}	$0.197^{+0.246}_{-0.102} \times 0.186^{+0.231}_{-0.096}$	-
151.0-00.4	8458	250719647917343232	1998^{+903}_{-643}	830^{+227}_{-136}	$0.920^{+0.416}_{-0.296} \times 0.727^{+0.328}_{-0.234}$	-
164.8-09.8	10890	176269718435866112	953^{+197}_{-109}	1250^{+137}_{-146}	$0.388^{+0.080}_{-0.044} \times 0.277^{+0.057}_{-0.032}$	-
174.6-05.2	8313	156214321404677376	3448^{+1086}_{-707}	3734^{+876}_{-578}	$6.270^{+1.974}_{-1.286} \times 4.096^{+1.290}_{-0.840}$	-
175.6+11.4	15571	955255358615209856	3960^{+1683}_{-1557}	1767^{+470}_{-318}	$2.419^{+1.028}_{-0.951} \times 2.419^{+1.028}_{-0.951}$	-
086.1+05.4	571	2179832585761932032	2389^{+543}_{-411}	1843^{+271}_{-179}	$2.259^{+0.514}_{-0.388} \times 2.143^{+0.487}_{-0.368}$	-

Table 4: Central stars with [Bailer-Jones et al. \(2021\)](#) distances, physical diameters from HASH angular diameters and r_{geo} , and GAIA DR3 radial velocities (where available).

IAU PNG	HASH ID	GAIA ID	r_{geo} [pc]	r_{phot} [pc]	physical diameter [pc]	v_{rad} [km s $^{-1}$]
086.9-03.4	15806	1970016153397634048	6192^{+1846}_{-1344}	8937^{+1603}_{-1598}	$0.991^{+0.295}_{-0.215} \times 0.600^{+0.179}_{-0.130}$	-
097.4+12.3	10889	2195278765626033024	3605^{+1502}_{-1353}	5237^{+3492}_{-1653}	$0.734^{+0.306}_{-0.275} \times 0.629^{+0.262}_{-0.236}$	-
109.4+07.7	4369	221879615111558016	3115^{+2702}_{-1230}	10382^{+2133}_{-1538}	$1.208^{+1.048}_{-0.477} \times 1.208^{+1.048}_{-0.477}$	-
183.0+00.0	9824	3430688759283627776	2803^{+777}_{-495}	2605^{+627}_{-443}	$0.219^{+0.061}_{-0.039} \times 0.219^{+0.061}_{-0.039}$	-

REFERENCES

- Acker A., Marcout J., Ochsenbein F., Stenholm B., Tylenda R., Schohn C., 1992, The Strasbourg-ESO Catalogue of Galactic Planetary Nebulae. Parts I, II.
- Acker A., Marcout J., Ochsenbein F., 1996, First Supplement to the Strasbourg-ESO Catalogue of Galactic Planetary Nebulae (SECGPN)
- Acker A., Boffin H. M. J., Outters N., Miszalski B., Sabin L., Le Dû P., Alves F., 2012, Rev. Mex. Astron. Astrofis., **48**, 223
- Bailer-Jones C. A. L., Rybizki J., Fouesneau M., Demleitner M., Andrae R., 2021, AJ, **161**, 147
- Baldwin J. A., Phillips M. M., Terlevich R., 1981, PASP, **93**, 5
- Chambers K. C., et al., 2016, arXiv e-prints, p. arXiv:1612.05560
- Chornay N., Walton N. A., 2021, A&A, **656**, A110
- Condon J. J., Cotton W. D., Greisen E. W., Yin Q. F., Perley R. A., Taylor G. B., Broderick J. J., 1998, AJ, **115**, 1693
- Dopita M. A., et al., 1997, ApJ, **474**, 188
- Drew J. E., et al., 2005, MNRAS, **362**, 753
- Frew D. J., Parker Q. A., 2010, Publ. Astron. Soc. Australia, **27**, 129
- Gaia Collaboration et al., 2016, A&A, **595**, A1
- Gaia Collaboration et al., 2022, arXiv e-prints, p. arXiv:2208.00211
- Gómez-González V. M. A., Mayya Y. D., Rosa-González D., 2016, MNRAS, **460**, 1555
- González-Santamaría I., Manteiga M., Manchado A., Ulla A., Dafonte C., López Varela P., 2021, A&A, **656**, A51
- Gunn J. E., et al., 1998, AJ, **116**, 3040
- Hajduk M., et al., 2021, ApJ, **919**, 121
- Hambly N. C., et al., 2001, MNRAS, **326**, 1279
- Jacoby G. H., et al., 2010, Publ. Astron. Soc. Australia, **27**, 156
- Kohoutek L., 2001, A&A, **378**, 843
- Kronberger M., et al., 2006, A&A, **447**, 921
- Kronberger M., et al., 2012, IAU Symposium, **283**, 414
- Kronberger M., et al., 2014, in Morisset C., Delgado-Ingla G., Torres-Peimbert S., eds, Asymmetrical Planetary Nebulae VI Conference. p. 48
- Kwitter K. B., Henry R. B. C., 2022, PASP, **134**, 022001
- Luridiana V., Morisset C., Shaw R. A., 2015, A&A, **573**, A42
- Maciel W. J., Costa R. D. D., 2003, in Kwok S., Dopita M., Sutherland R., eds, IAU Symposium Vol. 209, Planetary Nebulae: Their Evolution and Role in the Universe. p. 551
- Martin D. C., et al., 2005, ApJ, **619**, L1
- Miszalski B., Parker Q. A., Acker A., Birkby J. L., Frew D. J., Kovacevic A., 2008, MNRAS, **384**, 525
- Parker Q. A., 2022, Frontiers in Astronomy and Space Sciences, **9**, 895287
- Parker Q. A., et al., 2005, MNRAS, **362**, 689
- Parker Q. A., et al., 2006, MNRAS, **373**, 79
- Parker Q. A., Bojićić I. S., Frew D. J., 2016, in Journal of Physics Conference Series. p. 032008 (arXiv:1603.07042), doi:10.1088/1742-6596/728/3/032008
- Parker Q. A., Xiang Z., Ritter A., 2022, Galaxies, **10**, 32
- Ritter A., Parker Q. A., Lykou F., Zijlstra A. A., Guerrero M. A., Le Dû P., 2021, ApJ, **918**, L33
- Sabin L., et al., 2014, MNRAS, **443**, 3388
- Wright E. L., et al., 2010, AJ, **140**, 1868
- of rather narrow Galactic latitude range of ± 5 degrees then the best available on-line optical image is presented. After this there is then the mid-infrared WISE (Wright et al. 2010) 321 ($3.4\mu\text{m}$, $4.6\mu\text{m}$ and $12\mu\text{m}$ band combination) as an RGB image; the NVSS radio image (when available), (Condon et al. 1998) and finally the GALEX image when available, (Martin et al. 2005). Table A4 gives Images of the previously observed candidates that required better spectra for final confirmation in the same way as Table A3.

APPENDIX A: PNE IMAGES AND SPECTRA

In this appendix we conveniently provide a table of graphical images and spectra for all GTC PNe observations divided into 2 sub indices. Table A1 presents 1-D GTC spectra for the 55 new confirmed PNe; Table A2 gives Spectra of the previously observed candidates that required better spectra for final confirmation. Table A3 provides images of the 55 newly confirmed PNe. The table provides the IAU PNG ID; unique HASH ID number; an RGB optical image from the IPHAS H α , broad-band r and i data when available and then the quotient image from dividing the IPHAS H α by the broad-band r. If there is no IPHAS H α imagery available as the object falls outside

Table A1: Spectra of the 55 newly confirmed PNe.

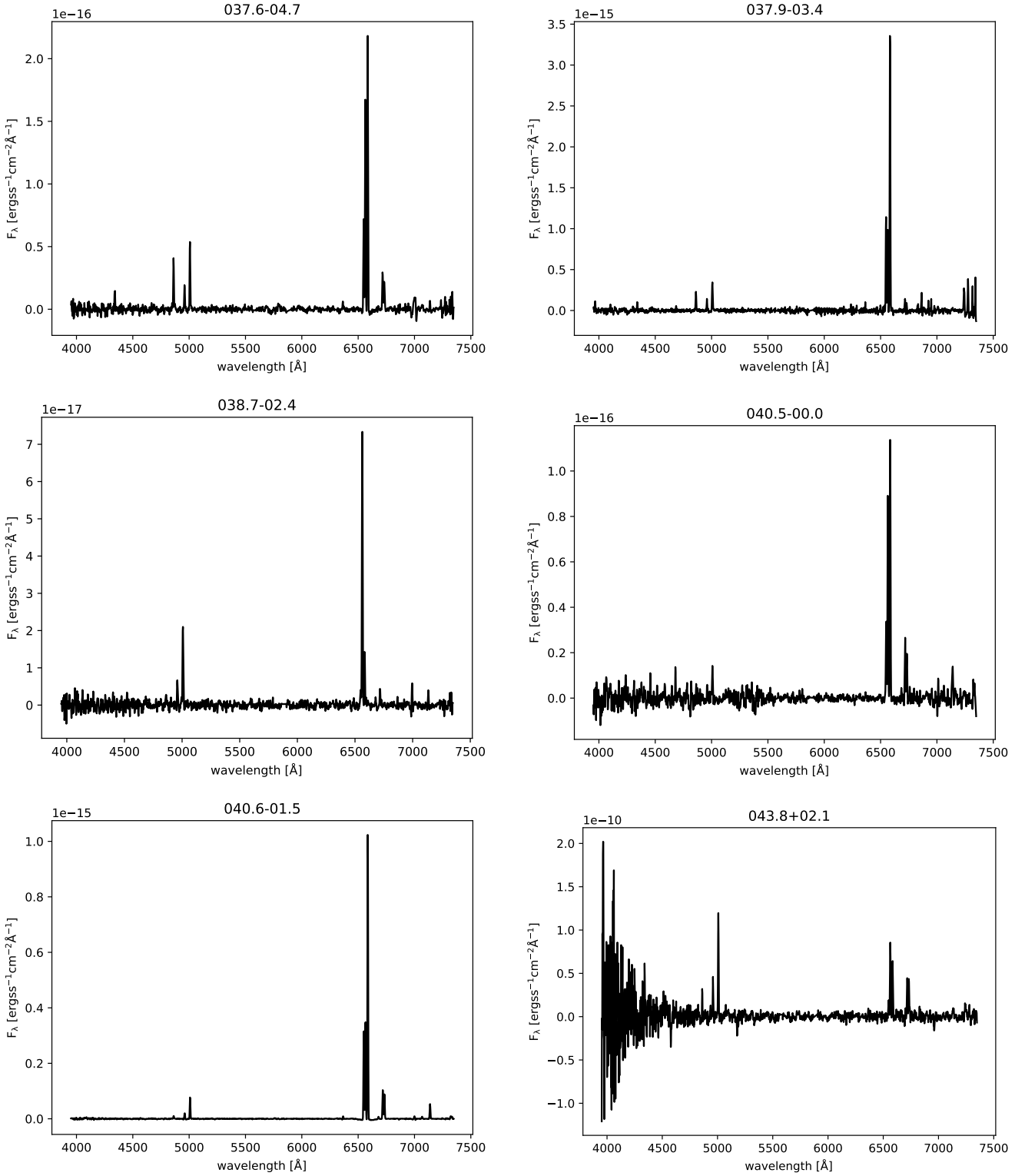


Table A1: Spectra of the 55 newly confirmed PNe.

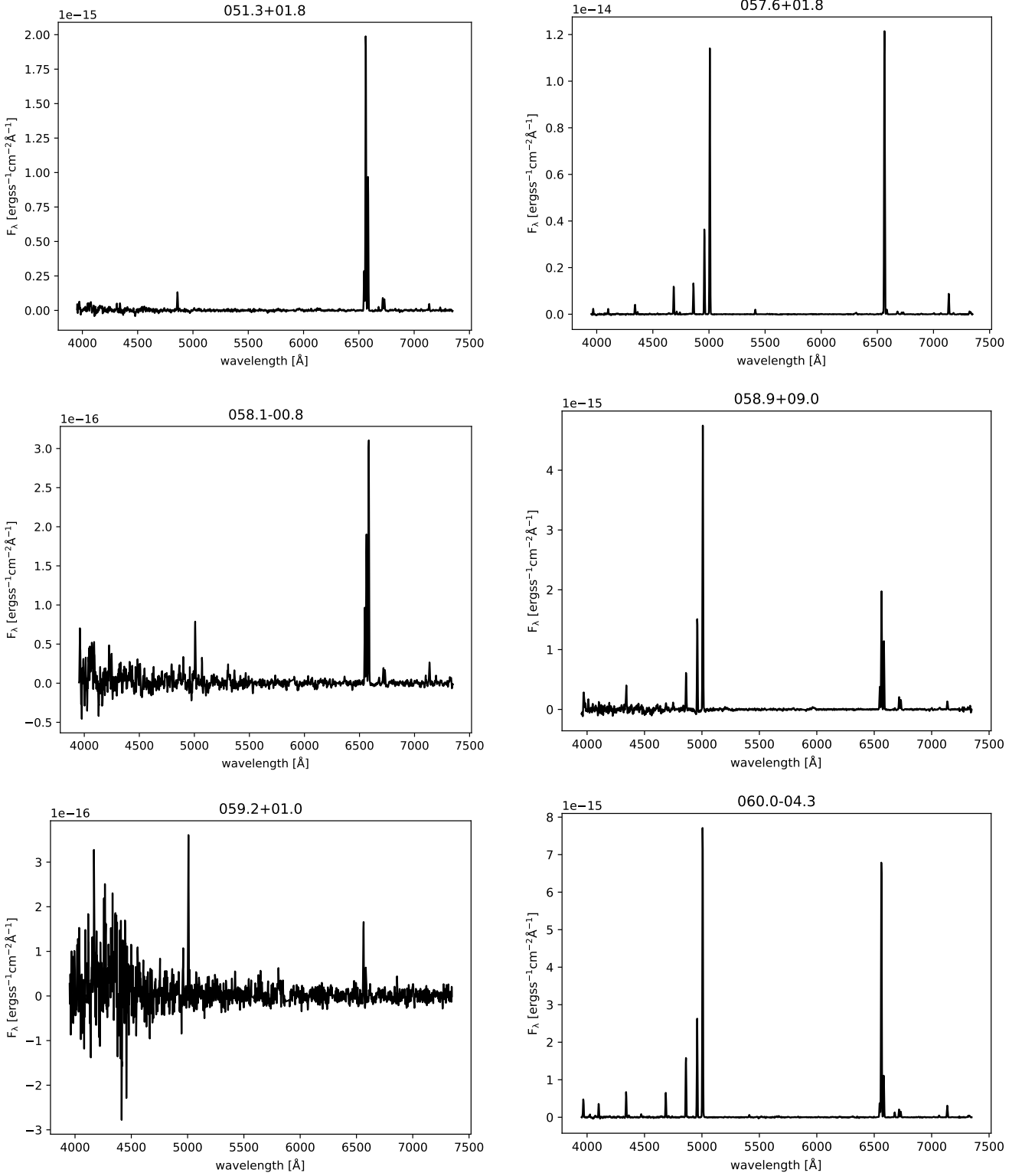


Table A1: Spectra of the 55 newly confirmed PNe.

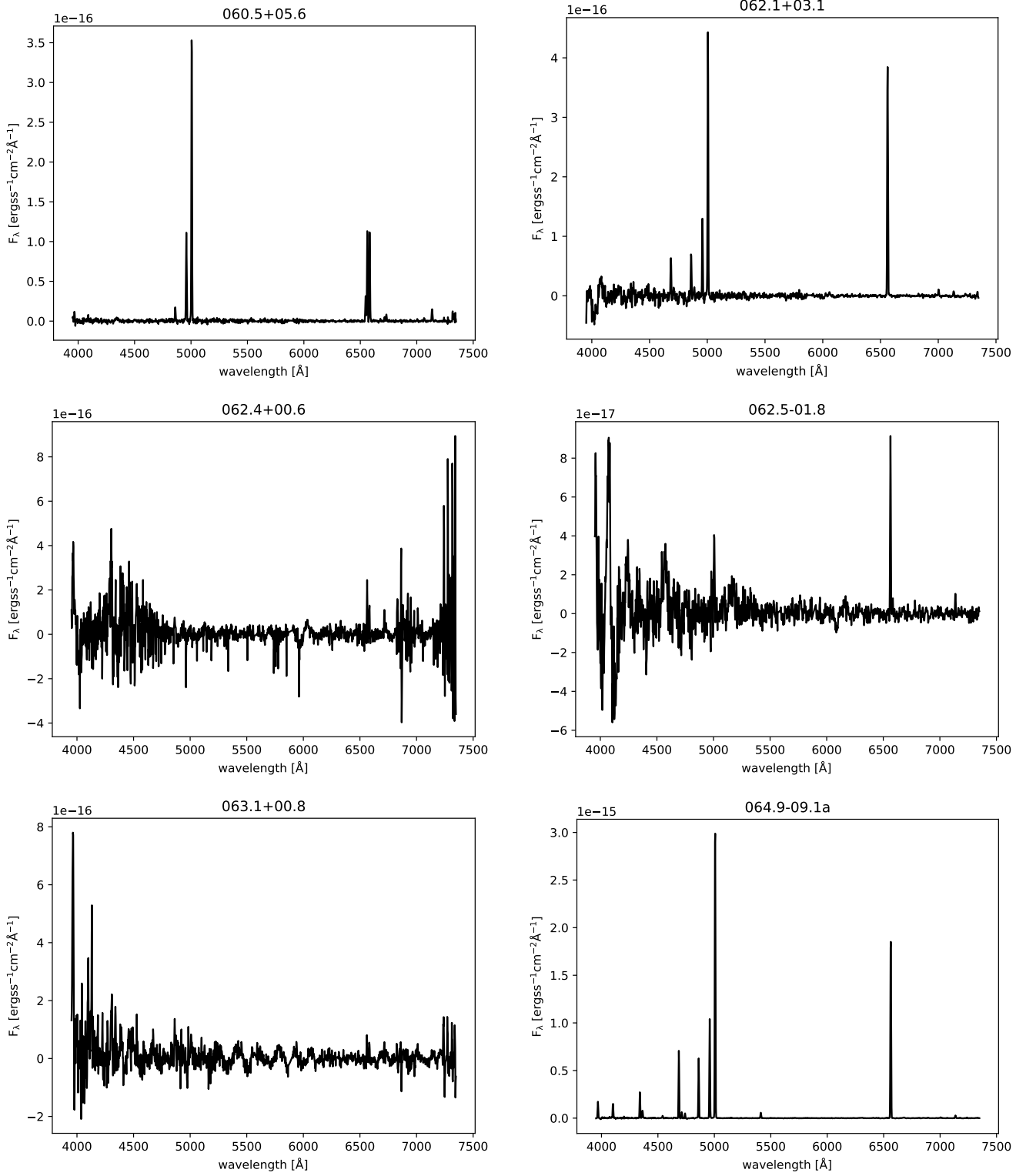


Table A1: Spectra of the 55 newly confirmed PNe.

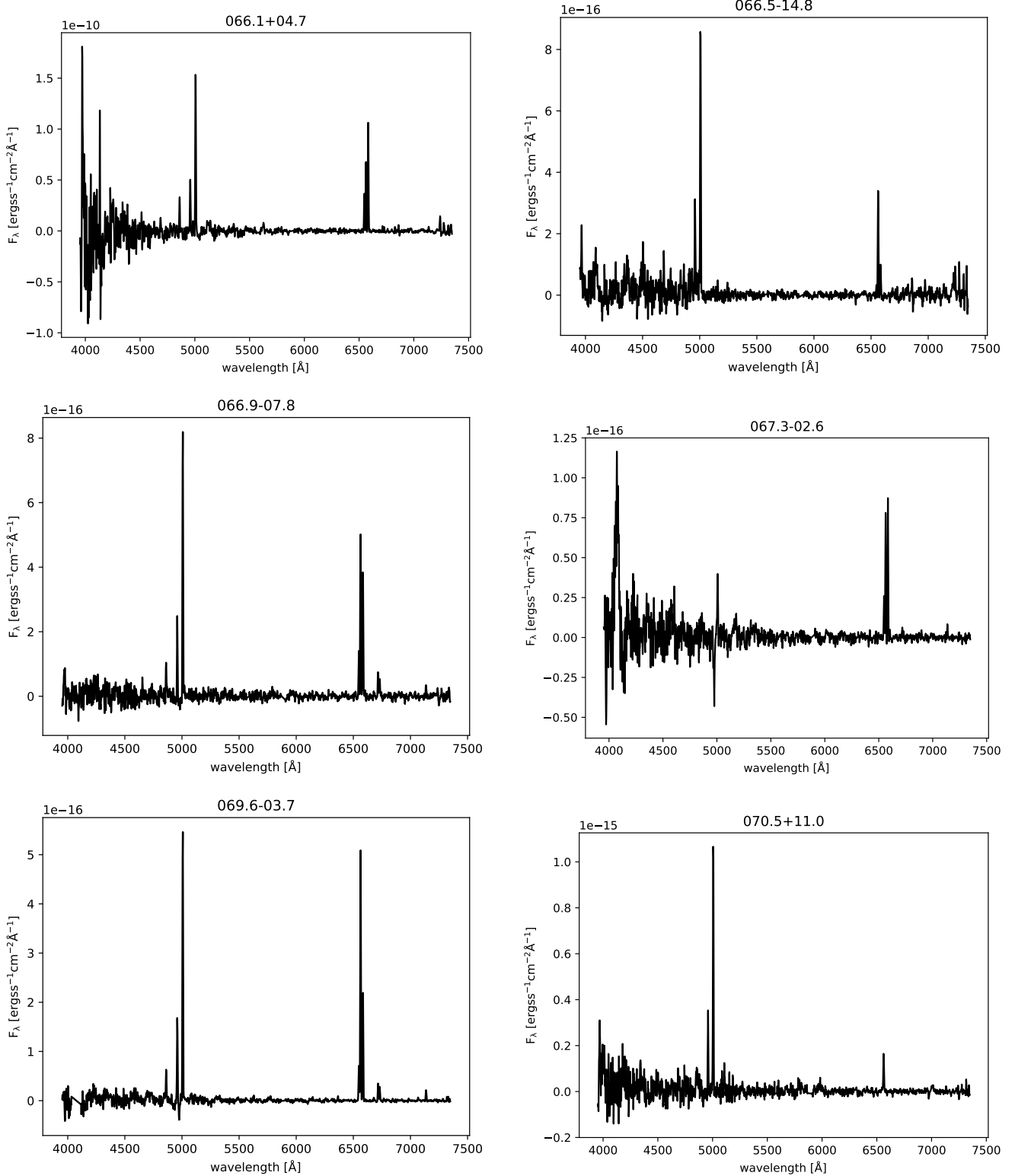


Table A1: Spectra of the 55 newly confirmed PNe.

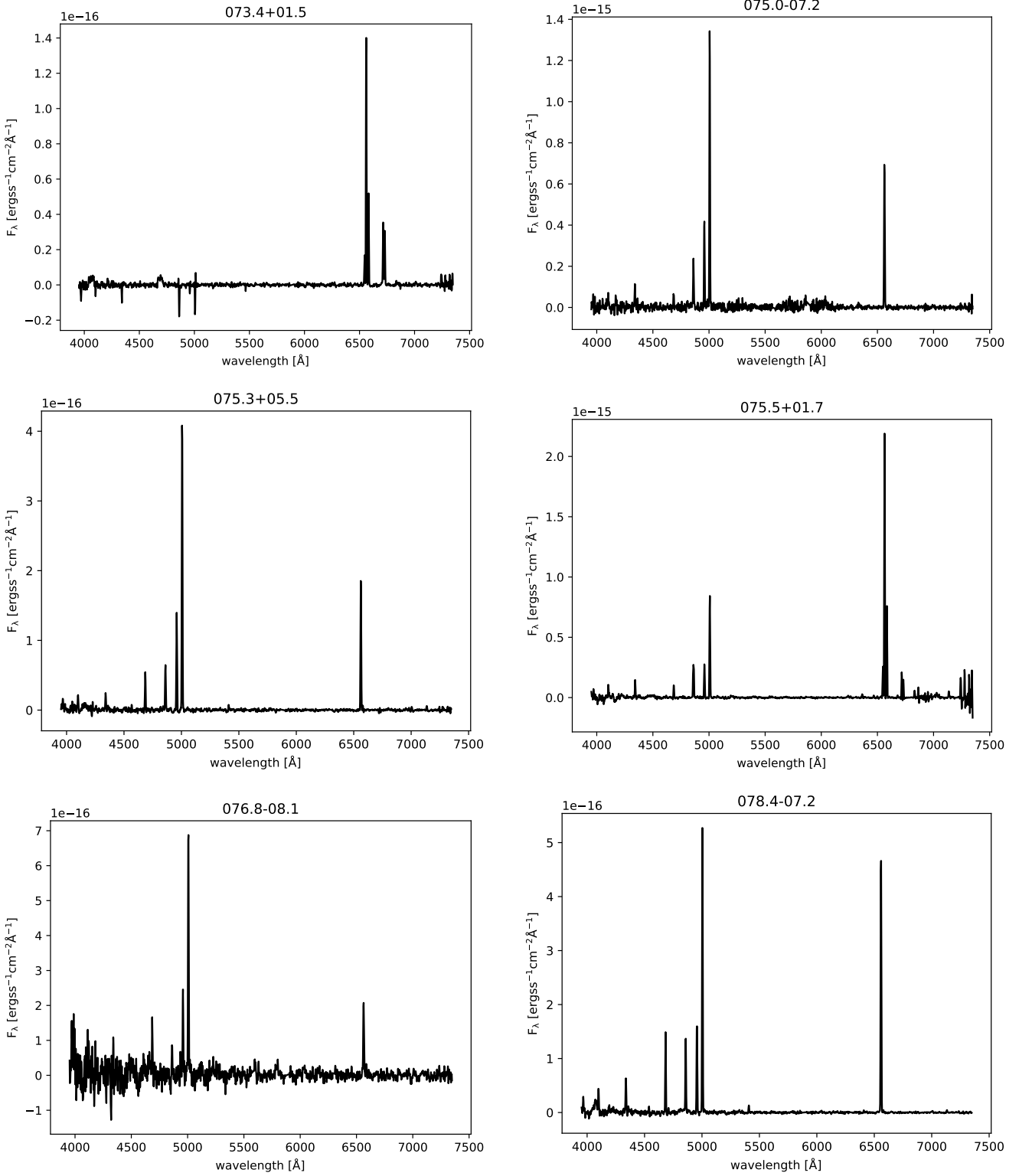


Table A1: Spectra of the 55 newly confirmed PNe.

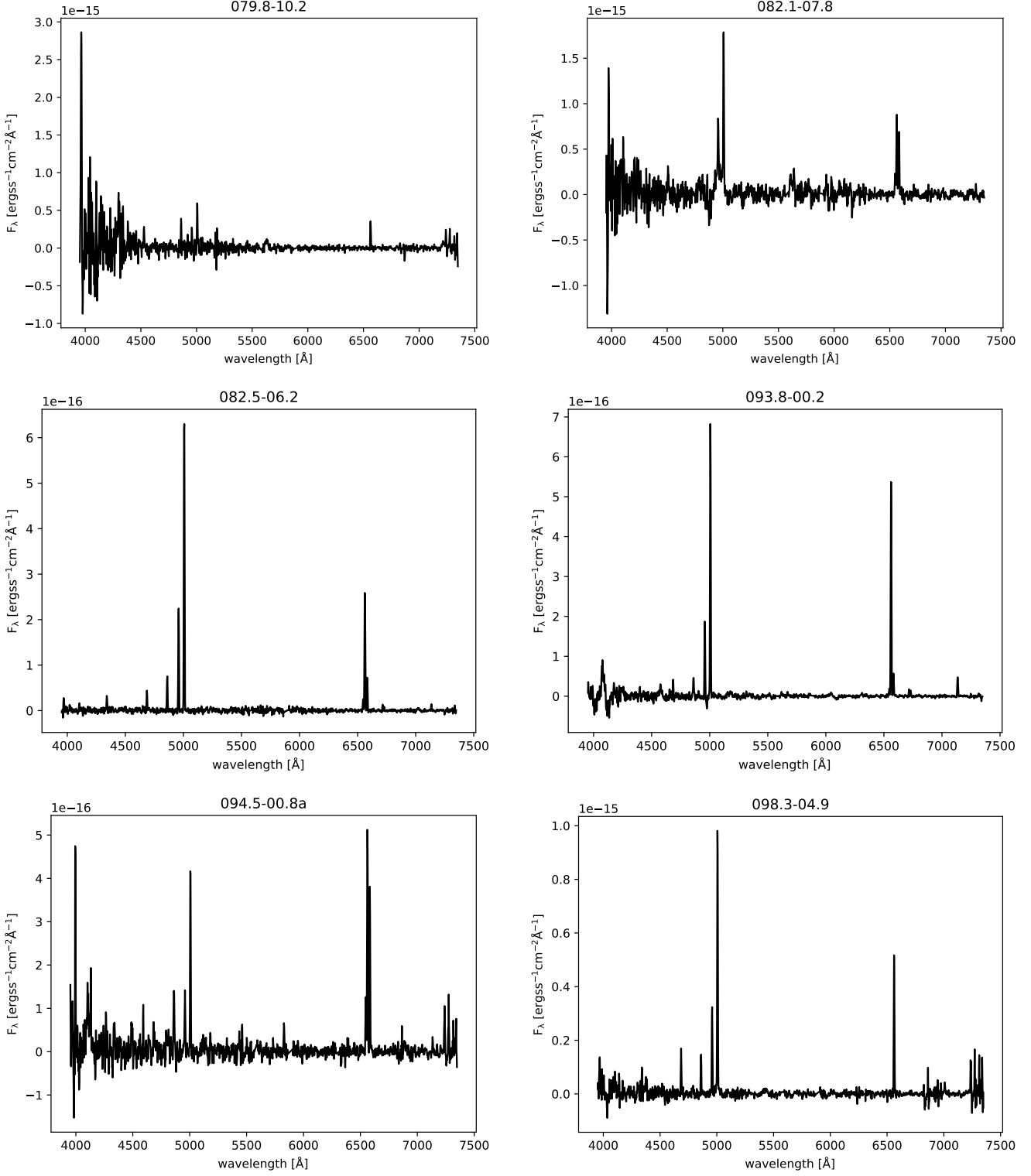


Table A1: Spectra of the 55 newly confirmed PNe.

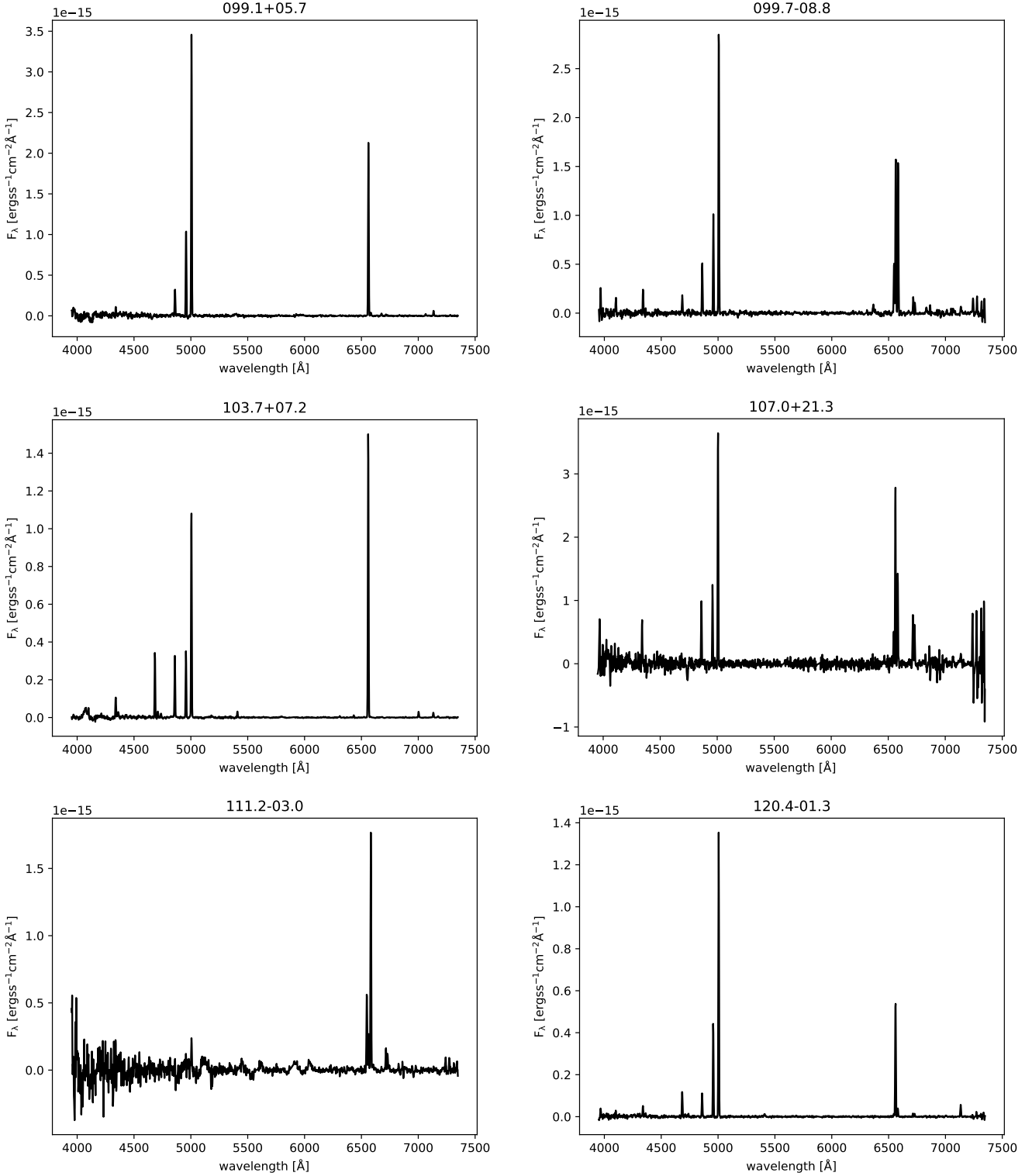


Table A1: Spectra of the 55 newly confirmed PNe.

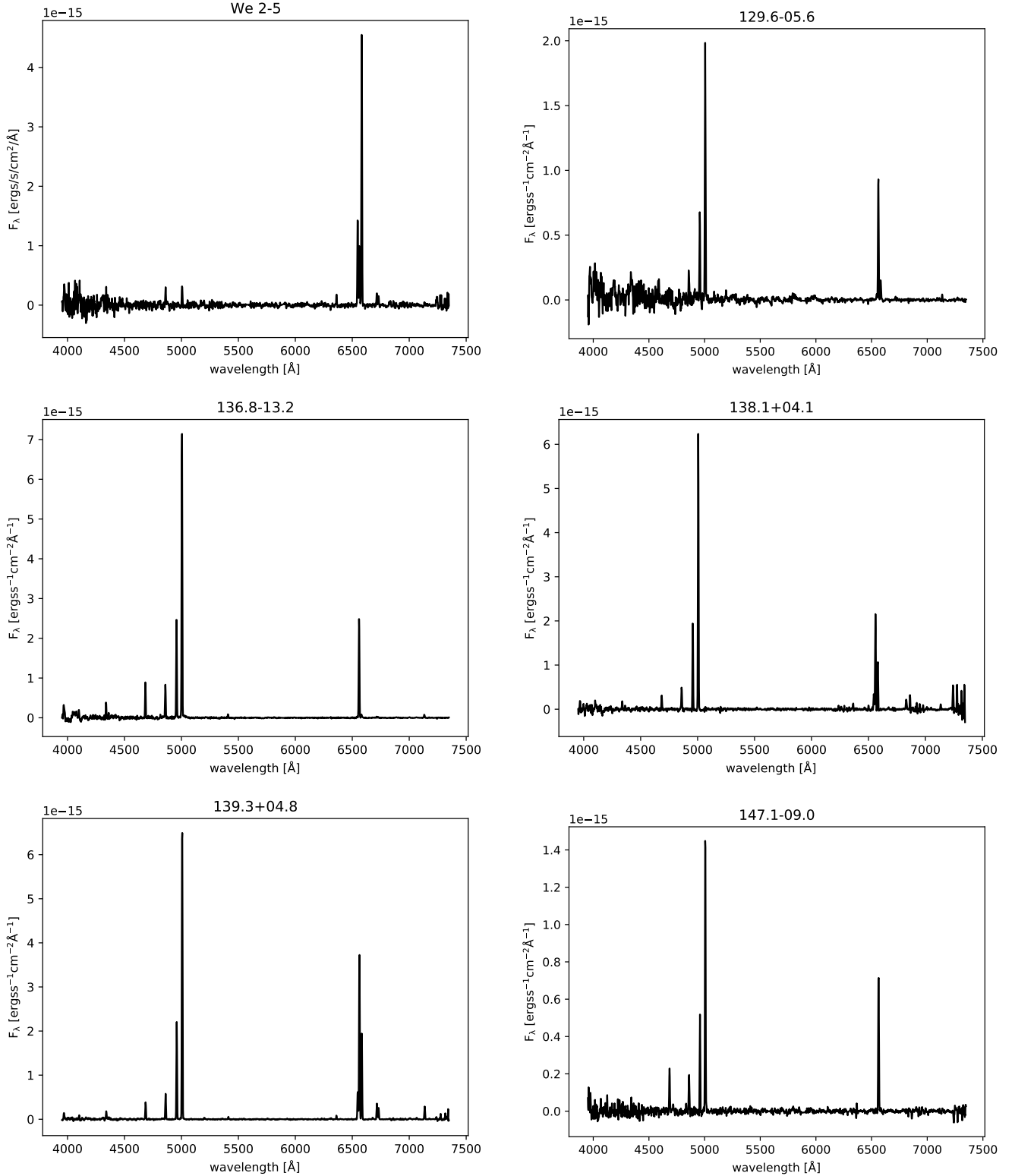


Table A1: Spectra of the 55 newly confirmed PNe.

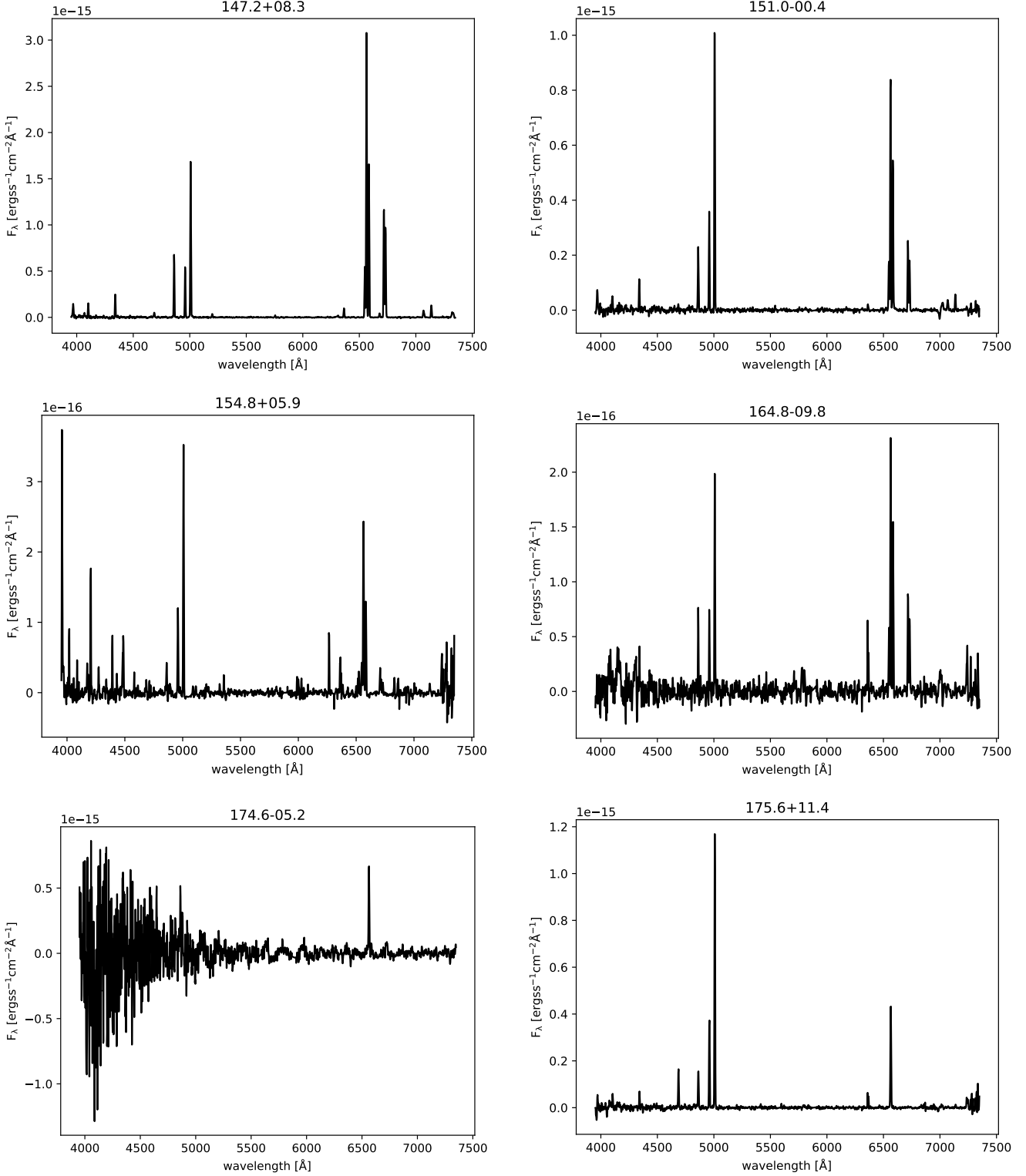


Table A1: Spectra of the 55 newly confirmed PNe.

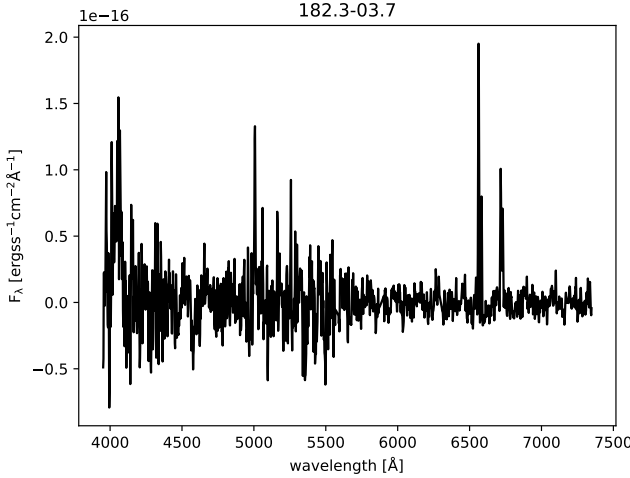


Table A2: Spectra of the previously observed candidates that required better spectra for final confirmation.

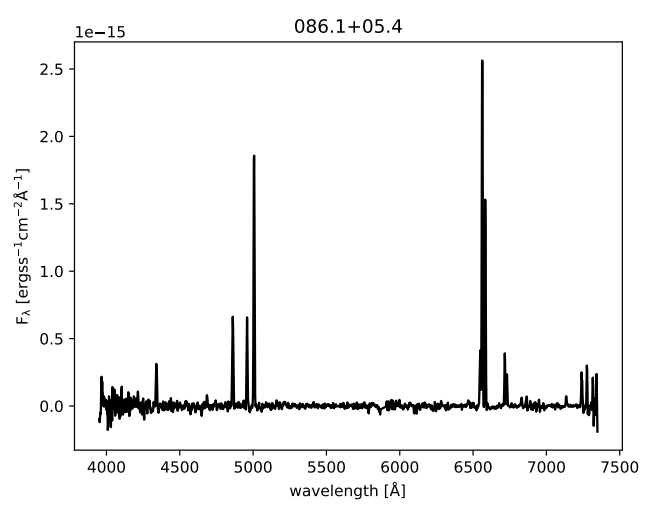
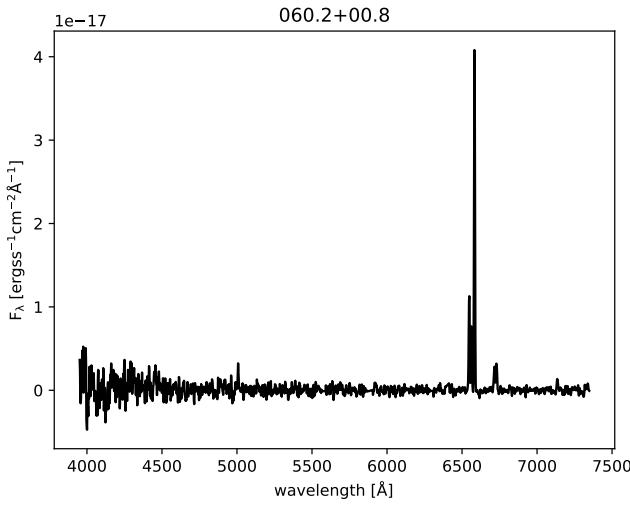
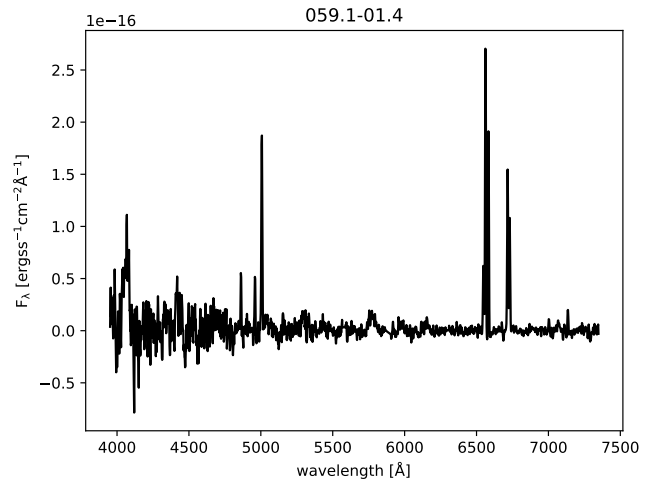
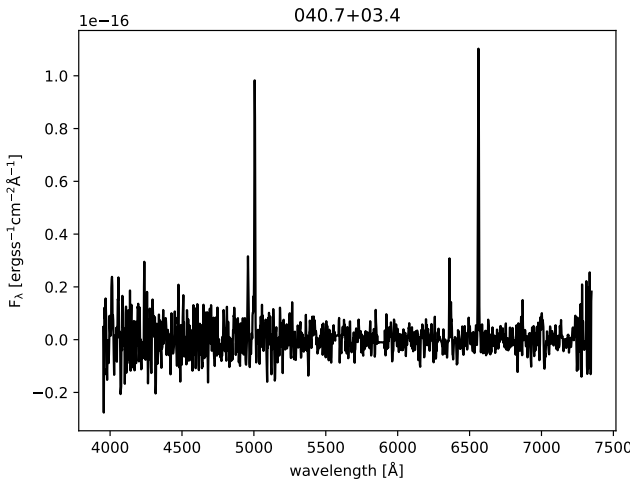


Table A2: Spectra of the previously observed candidates that required better spectra for final confirmation.

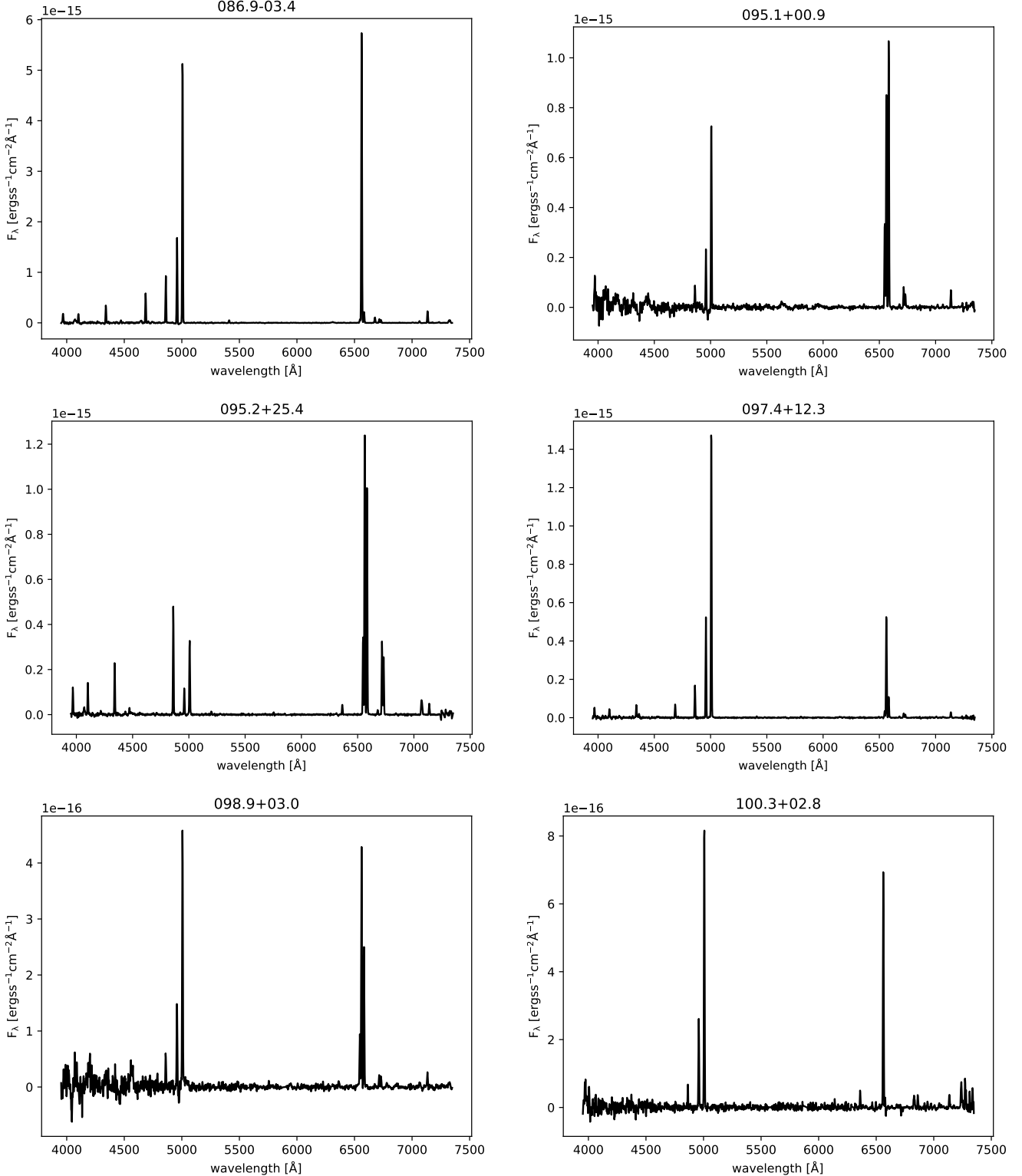


Table A2: Spectra of the previously observed candidates that required better spectra for final confirmation.

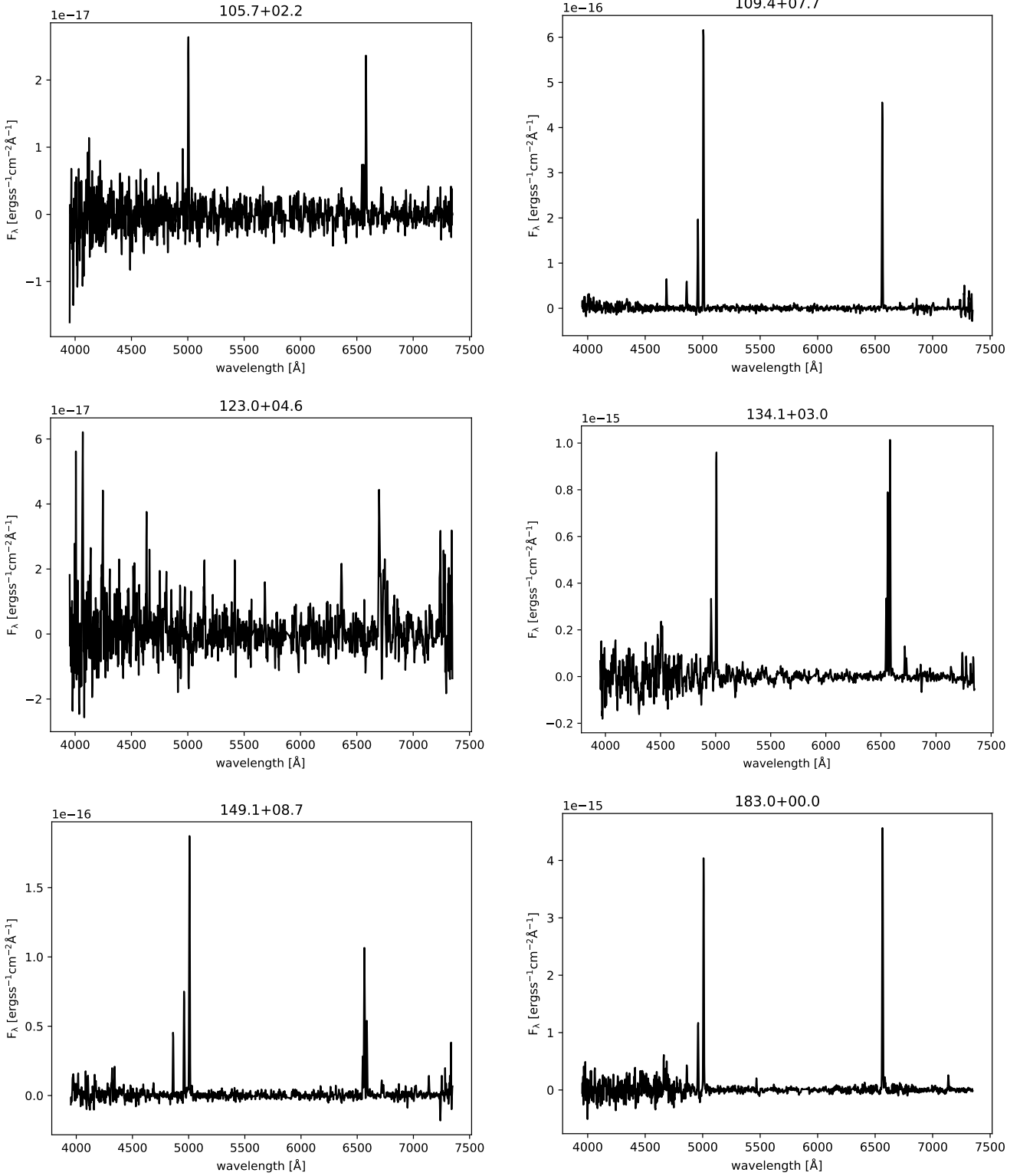


Table A3: Images of the 55 newly confirmed PNe. North is up and East is left.
The circles mark the major angular diameters given in the HASH database.

IAU PNG	HASH ID	optical	H_{α}/Sr	WISE321	NVSS	GALEX
037.6-04.7	2502					
037.9-03.4	390					
038.7-02.4	8193					
040.5-00.0	8190					
040.6-01.5	8528					
043.8+02.1	8506					
051.3+01.8	452					
057.6+01.8	4819					
058.1-00.8	8566					
058.9+09.0	486					

Table A3: Images of the 55 newly confirmed PNe. North is up and East is left.
The circles mark the major angular diameters given in the HASH database.

IAU PNG	HASH ID	optical	H_{α}/Sr	WISE321	NVSS	GALEX
059.2+01.0	10957					
060.0-04.3	495					
060.5+05.6	15561					
062.1+03.1	8206					
062.4+00.6	8214					
062.5-01.8	8219					
063.1+00.8	8217					
064.9-09.1a	15551					
066.1+04.7	8210					
066.5-14.8	4359					

Table A3: Images of the 55 newly confirmed PNe. North is up and East is left.
The circles mark the major angular diameters given in the HASH database.

IAU PNG	HASH ID	optical	H_{α}/Sr	WISE321	NVSS	GALEX
066.9-07.8	4356					
067.3-02.6	8232					
069.6-03.7	10881					
070.5+11.0	10899					
073.4+01.5	8230					
075.0-07.2	15564					
075.3+05.5	15565					
075.5+01.7	4408					
076.8-08.1	15566					
078.4-07.2	15567					

Table A3: Images of the 55 newly confirmed PNe. North is up and East is left.
The circles mark the major angular diameters given in the HASH database.

IAU PNG	HASH ID	optical	H_{α}/Sr	WISE321	NVSS	GALEX
079.8-10.2	10960					
082.1-07.8	560					
082.5-06.2	4362					
093.8-00.2	17066					
094.5-00.8a	10959					
098.3-04.9	15568					
099.1+05.7	4367					
099.7-08.8	602					
103.7+07.2	4368					
107.0+21.3	617					

Table A3: Images of the 55 newly confirmed PNe. North is up and East is left.
The circles mark the major angular diameters given in the HASH database.

IAU PNG	HASH ID	optical	H_{α}/Sr	WISE321	NVSS	GALEX
111.2-03.0	8266					
120.4-01.3	10956					
129.2-02.0	655					
129.6-05.6	658					
136.8-13.2	10896					
138.1+04.1	670					
139.3+04.8	4393					
147.1-09.0	4495					
147.2+08.3	4330					
151.0-00.4	8458					

Table A3: Images of the 55 newly confirmed PNe. North is up and East is left.
The circles mark the major angular diameters given in the HASH database.

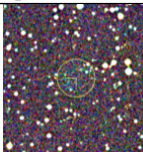
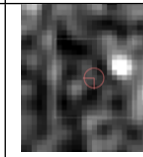
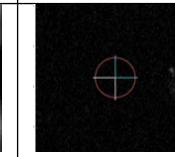
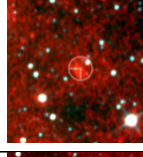
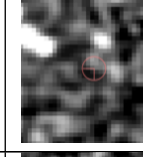
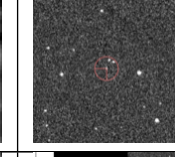
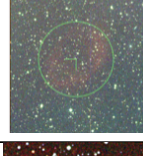
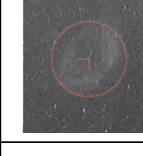
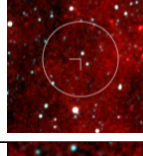
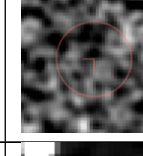
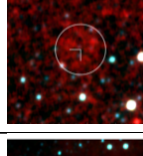
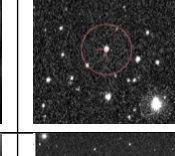
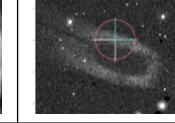
IAU PNG	HASH ID	optical	H_{α}/Sr	WISE321	NVSS	GALEX
154.8+05.9	4333					
164.8-09.8	10890					
174.6-05.2	8313					
175.6+11.4	15571					
182.3-03.7	8331					

Table A4: Images of the previously observed candidates that required better spectra for final confirmation. North is up and East is left. The circles mark the major angular diameters given in the HASH database.

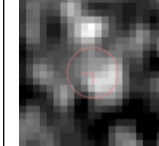
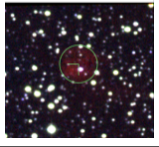
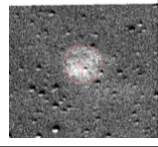
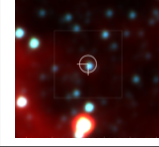
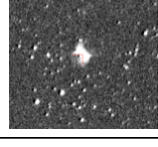
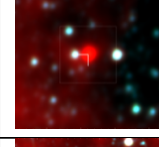
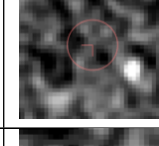
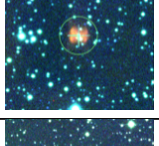
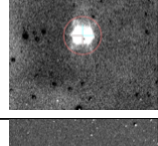
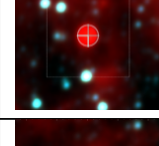
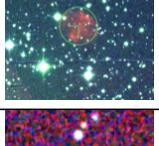
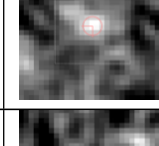
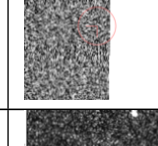
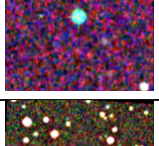
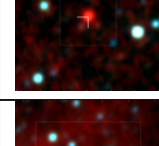
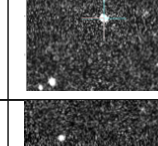
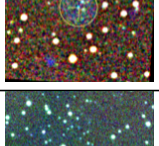
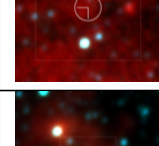
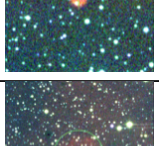
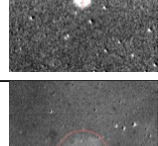
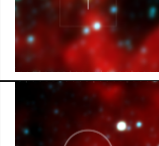
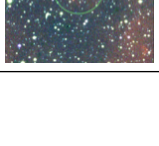
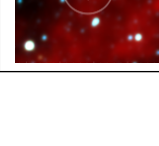
IAU PNG	HASH ID	optical	H_{α}/Sr	WISE321	NVSS	GALEX
040.7+03.4	4424					
059.1-01.4	8215					
060.2+00.8	10878					
086.1+05.4	571					
086.9-03.4	15806					
095.1+00.9	4431					
095.2+25.4	10897					
097.4+12.3	10889					
098.9+03.0	10285					
100.3+02.8	4386					

Table A4: Images of the previously observed candidates that required better spectra for final confirmation. North is up and East is left. The circles mark the major angular diameters given in the HASH database.

IAU PNG	HASH ID	optical	H_{α}/Sr	WISE321	NVSS	GALEX
105.7+02.2	5240					
109.4+07.7	4369					
123.0+04.6	15569					
134.1+03.0	4425					
149.1+08.7	4332					
183.0+00.0	9824					

This paper has been typeset from a $\text{\TeX}/\text{\LaTeX}$ file prepared by the author.